

**Petrography and geochemistry of the Mesoarchean Bikoula banded iron formation in the Ntem complex (Congo craton), Southern Cameroon: Implications for its origin**

Tessontsap Teutsong<sup>a,b,\*</sup>, Tomaso R.R. Bontognali<sup>b</sup>, Paul-Désiré Ndjigui<sup>a</sup>, Johannes C. Vrijmoed<sup>b</sup>, Damon Teagle<sup>c</sup>, Matthew Cooper<sup>c</sup>, Derek Vance<sup>b</sup>

<sup>a</sup> *Department of Earth Sciences, University of Yaoundé I, Cameroon*

<sup>b</sup> *Institute of Geochemistry and Petrology, ETH Zurich, Switzerland*

<sup>c</sup> *Ocean and Earth Science, National Oceanography Centre Southampton, University of Southampton, United Kingdom*

\*Corresponding author: tessontsap@yahoo.fr / tessontsap.teutsong@uy1.uninet.cm

**Abstract**

Precambrian banded iron formations (BIFs) represent an important source of mineable iron, as well as an archive recording secular changes in the chemistry of the Earth's early oceans. Here we report petrographic and geochemical characteristics of unweathered drill core samples from the Bikoula BIF, a virtually uncharacterized oxide facies iron formation, hosted in the Mesoarchean Ntem complex, southern Cameroon. The BIF is cross-cut with syenitic veins. The entire succession is highly deformed and metamorphosed under granulite facies conditions. The BIF is characterized by alternating micro-bands of magnetite, quartz and pyroxene. Sulfides (pyrite, pyrrhotite, and chalcopyrite), oligoclase, ferro-pargasite, biotite and ilmenite occur as minor phases. The presence of pyroxene, ferro-pargasite and oligoclase, relatively high contents of major elements such as Al<sub>2</sub>O<sub>3</sub> (0.76 – 7.52 wt.%), CaO (1.95 – 4.90

wt.%), MgO (3.78 – 5.59 wt.%), as well as positive correlations among Al<sub>2</sub>O<sub>3</sub>, TiO<sub>2</sub>, HFSEs, LILEs and transition metals (V, Cr, Ni, Cu and Zn), suggest that the BIF protolith included a significant amount of clastic material. Several samples have preserved seawater-like PAAS-normalized REE-Y patterns, including LREE depletion, and positive La and Y anomalies. Positive Eu anomalies observed in some of the analyzed samples indicate influx of hydrothermal fluids (possibly including Fe and Si) within the basin where the BIF precipitated. However, few samples show unusual negative Eu anomalies that likely result from a large proportion of clastic contamination. The lack of Ce anomalies suggests that the Bikoula BIF was deposited in a basin that was (at least partly) anoxic or suboxic, where it was possible to transport and concentrate dissolved Fe<sup>2+</sup>.

**Keywords:** Bikoula BIF; Ntem complex; Granulite-facies metamorphism; Hydrothermal fluids; Seawater

## 1. Introduction

Banded iron formations (BIFs) are chemical sedimentary rocks that contain  $\geq 15\%$  iron and typically display banding consisting of iron-rich layers alternating with silica-rich layers (James, 1954; Trendall, 2002). BIFs are common in the Precambrian geological record, while an equivalent facies has never been observed in Phanerozoic sequences or modern environments (Klein, 2005). BIFs are of great interest due to their economic importance as the world's largest source of iron ore (Robb, 2005), and because the models proposed to explain their genesis are intimately linked to the evolution of the Earth's atmosphere, hydrosphere, and biosphere (Konhauser et al., 2009; Bontognali et al., 2013). Based on their depositional environment and co-occurring rock facies, BIFs have been subdivided into Superior- and Algoma-types (Gross, 1980). The former were deposited in near-shore continental shelf environments and are associated with carbonates, quartzites and black shales, whereas the latter

are consistently associated with volcanic rocks and greywackes in greenstone belts. All BIFs have experienced some form of diagenetic and/or metamorphic overprinting (Klein, 2005), which makes it challenging to unambiguously reconstruct the precise depositional setting and the paleoenvironment in which the iron-bearing minerals originally precipitated.

Despite decades of research, many fundamental questions about the origin of BIFs remain unanswered and highly debated. However, some common concepts recur in most of the proposed hypotheses. It is commonly thought that, during the period of BIFs deposition, the oceans (at least at depth) were anoxic, and thus capable of transporting and accumulating dissolved ferrous iron (Cloud, 1968; Holland, 1973). The latter may have been oxidized to solid-phase iron oxyhydroxides through either biological (oxygenic or anoxygenic photosynthesis) or nonbiological (ultraviolet photo-oxidation) processes (Bekker et al., 2014). Alternatively, direct precipitation under anoxic conditions may have formed Fe-carbonates or mixed valence Fe-silicates. Based on REE distributions, it has been proposed that Fe and Si in most BIFs derive from hydrothermal sources (Holland, 1973; Bau and Möller, 1993; Morris and Horwitz, 1983), although Hamade et al. (2003) used Ge/Si ratios in BIFs to postulate a continental source for silica.

This study focuses on the Bikoula BIF, an Algoma-type iron formation hosted in the Mesoarchean Ntem complex, which constitutes the northwestern edge of the Congo craton (Maurizot et al., 1986). Several greenstone belt occurrences hosting BIFs of economic importance have been identified in the Ntem complex (Maurizot et al., 1986). However, previous studies of BIFs in this region exclusively focused on weathered BIFs that crop out at the surface (Lerouge et al., 2006; Suh et al., 2008, 2009; Nforba et al., 2011; Ilouga et al., 2013; Chombong et al., 2013; Anderson et al., 2014; Ganno et al., 2015, 2016), where weathering makes it difficult to reliably understand their petrogenesis. Here, we present the first petrographic and geochemical data on unweathered BIF and cross-cutting rocks of the Ntem

complex, which were collected in the framework of a drilling project named the Bikoula Iron Ore Project (Aluvance Plc, 2014). The presented data are compared, discussed and interpreted with regard to previous studies of BIFs.

## **2. Geological setting**

### **2.1. Regional geology**

The Ntem complex corresponds to the northwestern border of the Congo craton in Southern Cameroon (Maurizot et al., 1986). It is bounded to the north by the Yaoundé Group which belongs to the Pan-African orogenic belt in Central Africa (Nédélec et al., 1986; Nzenti et al., 1988). The Ntem complex has been subdivided into three units: Ntem, Nyong and Ayna.

The Ntem unit contains the Bikoula BIF (Fig. 1) and comprises an intrusive series, a banded series and greenstone belts (Maurizot et al., 1986; Pouclet et al., 2007). The intrusive series occurs in the northern part and consists dominantly of magmatic charnockitic suite and TTG (Tonalite-Trondjemite-Granodiorite) suite (Pouclet et al., 2007). The banded series is represented by highly deformed granulitic gneisses (leptynites, enderbergites, granitic gneisses and charnockitic gneisses) that are distributed over the southern part of the Ntem unit (Maurizot et al., 1986; Takam et al., 2009).

Greenstones in the Ntem unit occur as disrupted belts and as xenoliths in the intrusive series, indicating an older age for their formation (Shang et al., 2004a, 2007). These supracrustal rocks consist of BIFs, metagraywackes, sillimanite-bearing paragneisses, garnet-bearing amphibolites and pyroxenites (Shang et al., 2004a; Tchameni et al., 2010). They were affected by granulite-facies metamorphism with estimated peak temperatures of  $750 \pm 50$  °C at 5 – 6 kbar (Tchameni, 1997; Tchameni et al., 2001). Emplacement of the greenstone belts in the Ntem unit has been dated at ca. 3.1 Ga using the Pb-Pb zircon evaporation technique (Tchameni et



al., 2004). Greenstone belts are highly dismembered and cross-cut by late syenitic plutons and doleritic veins (Tchameni et al., 2001).

The Ntem complex was affected by two major periods of deformation. The first involves successive diapiric emplacements of the Mesoarchean charnockites (~ 2.900 Ma) and TTGs (~ 2830 Ma). It is marked by vertical foliation and lineation, stretching and isoclinal folds (Shang et al., 2004a). This episode of deformation was synchronous with a regional granulite-facies metamorphism (Tchameni, 1997). This Archean event was followed, in the Paleoproterozoic, by a transcurrent deformation phase marked by the development of N-S to NE-SW trending sinistral shear zones and partial melting of the TTG suite and the greenstone belt country rocks, with generation of a variety of granites (Shang et al., 2007). Late syenitic plutons (~ 2.3 Ga) intruded the complex during this second tectonic episode (Tchameni et al., 2001). The Eburnean metamorphism affected all the Archean and Paleoproterozoic formations and was dated at ~ 2.05 Ga (Toteu et al., 1994).

## **2.2. Local geology and stratigraphy**

In the Bikoula region, the BIF ore bodies occur in roughly NW-SE direction with steep dips 50–80° to the SW or NE (Fig. 2). The main ore body is ~0.5 km in width and extends ~4.8 km along strike. The country rocks in the Bikoula area are pyroxene-bearing granitoids (charnockites) of various orientations. Observations at outcrops typically reveal highly weathered BIF with characteristic light (silica) bands alternating with dark (iron oxide) bands (Fig. 3). Analysis of remote sensing data revealed E-W and NE-SW trending faults/shear zones that affected both ore bodies and country rocks, resulting in mylonitic structures observed in many outcrops.

A vertical drill core (BKLD030), of ~133.8 m deep, through the central part of the main ore body (Fig. 2) was chosen for this study. It comprises various iron ore formations cross-cut

by syenitic veins (Fig. 4). The lower part of the core comprises unweathered BIF which grades upwards into partly oxidized and altered sheared BIF. The uppermost part of the sheared BIF has been affected by weathering and oxidation processes resulting in a sheared oxidized BIF. Close to the topographic surface, intense weathering and erosional processes prevailed and generated supergene high-grade ores namely the soft saprolitic and detrital ores. Because the middle and upper parts of the core were affected by secondary enrichment through intensive shearing and weathering processes, the present study exclusively focuses on the unweathered lower part of the drill core.

### 3. Sampling and analytical procedures

Samples were selected from a split diamond core and were then halved using a core cutting machine (quarter thickness of the whole original core). The length of samples was variable depending on the scale of banding, the compositional homogeneity and the thickness of individual rock units. From the sampled quarter, polished thin sections were cut perpendicular to the banding and the remainder of the core was crushed for geochemical analyses. A total of 12 unweathered BIF samples and 11 of the syenites were collected for petrographic and geochemical investigations (Fig. 4).

Detailed petrographic observations were undertaken using transmitted and reflected light microscopy on polished thin sections at ETH Zurich, Switzerland, where a JEOL JXA-8200 electron microprobe analyzer was utilized for mineral analyses. Natural and artificial silicates and oxides were used as standards. An acceleration voltage of 15 kV was used, along with 20 nA beam current and 20  $\mu\text{m}$  beam diameter. Measuring time on the peak was 40 seconds, with 10 seconds on the background. The detection limit was approximately 0.01 wt.% for major and minor elements, and relative measurement errors did not exceed 1%. A Jeol JSM-6390 LA scanning electron microscope (SEM), equipped with a secondary electron (SE) and a

backscatter electron detector (BSE), was used to examine textural relationships of extremely fine mineral phases.

Major element concentrations in BIF samples were analyzed using an Axios FAST X-ray fluorescence spectrometer with an RSD (Relative Standard Deviation) < 5% at the ALS laboratory (Ireland), and in the syenites with a wavelength dispersive X-ray fluorescence spectrometer (WD-XRF, PANalytical AXIOS) at ETH Zurich. Trace element analyses of BIF samples were performed using an ICP-MS (Element, Finnigan MAT) at ETH Zurich. Rare earth elements were acquired using a ThermoFisher XSeries 2 ICP-MS at University of Southampton. The RSD was < 2.5% for the trace and REE analyses.

## **4. Petrography**

### **4.1. BIF**

At the mesoscopic scale, BIF shows a conspicuous banding (Fig. 5a). Banding is generally irregular in thickness and obliterated in places. The BIF is generally characterized by intercalated quartz-rich grey-white and magnetite-rich dark bands or laminae. Between these bands (i.e. light and dark bands), a pyroxene-rich greenish brown layer often occurs, imparting a greenish coloration to the BIF. Contacts between the laminae are usually diffuse. The magnetite-rich and pyroxene-rich bands are highly magnetic. The main minerals are quartz (30 – 40 vol.%), magnetite (30 – 50 vol.%) and pyroxene (20 – 30 vol.%), with smaller amounts of plagioclase, amphibole, biotite, ilmenite and sulfides.

#### **4.1.1. Quartz**

Quartz occurs as aggregates in quartz-rich bands or individual grains within the magnetite- and pyroxene-rich bands, and is often found as inclusions in grains of pyroxene (Fig. 5b). In these bands, quartz occurs as anhedral, up to 2.5 mm in size, slightly elongated grains

with moderate preferred orientation (Figs. 5c–d). Quartz is often intermixed with magnetite and pyroxene, resulting in a weaker banding of the BIF. Many quartz grains exhibit inequigranular interlobate texture, display undulose extinction and embayed to amoeboid grain boundaries. Larger grains commonly show patchy extinction resulting from the coalescence of smaller subgrains. All these deformational features are suggestive of dynamic recrystallization.

#### **4.1.2. Pyroxene**

Pyroxene occurs as orthopyroxene and clinopyroxene in approximately equal proportions. Orthopyroxene is brownish in color, anhedral to subhedral, and forms bands of variable thickness that appear to alternate with quartz and magnetite bands (Fig. 5b). The orthopyroxene bands range from 1.5 to 2 mm in thickness and are not continuous, often cross-cut by magnetite or quartz. Most orthopyroxene occurs as medium to coarse grains up to 4 mm in length and 2.4 mm wide and often show preferred orientation. The large grains contain inclusions of clinopyroxene, magnetite and sulfides. Grain boundaries are generally embayed to smoothly curved against other minerals. Smaller crystals can be found associated with both the magnetite and quartz-rich laminae. Exsolution lamellae of clinopyroxene as well as deformation twins are clearly visible in many grains (Fig. 5d).

Clinopyroxene is noticeably smaller, reaching 1.5 mm in length for the larger grains, and occurs as anhedral to subhedral crystals. In thin section, grains appear scattered, are commonly in contact with magnetite and orthopyroxene bands, and display a preferred orientation in places. Clinopyroxene is pale green, non pleochroic, with yellow-orange to blue-purple interference colors, and exhibits straight to curved grain outlines (Fig. 5d). Some clinopyroxene crystals display simple twinning. Extremely fine orthopyroxene exsolution lamellae are common in many crystals. Two generations of clinopyroxene occur, the first as

porphyroblasts containing exsolution lamellae of orthopyroxene (Fig. 5d) and the second as small anhedral crystals in large cracks of orthopyroxene megacrysts (Fig. 5e).

#### **4.1.3. Magnetite**

Magnetite, the main iron mineral of the Bikoula BIF, occurs in 1.5–3.5 mm thick bands. Within the magnetite-rich layers, magnetite exhibits a texture consisting of continuously interlocking grains (Figs. 6a–b). Fe-rich layers display many cracks where magnetite is often partially replaced by pyrite (Fig. 6c). In quartz and pyroxene bands, magnetite grains are subhedral to euhedral in shape, and may be distributed rather uniformly, or interconnected to form aggregates of various configurations (see Fig. 5b). Grain boundaries shared with the other minerals are straight to smoothly curved. Magnetite is also found as inclusions or in contact with grains of quartz and pyroxene.

#### **4.1.4. Minor mineral phases**

Sulfides in the Bikoula BIF comprise pyrite, pyrrhotite and subordinate chalcopyrite. Pyrite occurs as subhedral to euhedral crystals interstitial to magnetite and pyroxene, and displays straight to smoothly curved contacts with the latter two minerals (Fig. 6a). Pyrite grains are irregularly shaped with a random arrangement, and may range up to 0.5 mm in size. Most pyrite crystals are partially to completely replaced by pyrrhotite (Figs. 6c–d), indicating sulphur release during progressive metamorphism (Craig and Vokes, 1993). Pyrite often contains very fine inclusions of chalcopyrite and magnetite. Chalcopyrite grains are anhedral to subhedral,  $\leq 20 \mu\text{m}$  in size, and commonly associated with pyrite (Fig. 6d).

Plagioclase occurs as anhedral to subhedral grains, up to 4 mm, that display undulose extinction (Figs. 6e–f). It often contains minute inclusions of magnetite. Amphibole forms strongly pleochroic greenish to brownish colored individual crystals. Mineral grains present vary from anhedral to subhedral and reach up to 2.8 mm in size. Locally, the mineral is slightly

altered to Fe-rich biotite (Fig. 6e), and often contains inclusions of magnetite and plagioclase. Biotite occurs mostly as aggregates that are bent or kinked, presumably due to tectonic overprint. Crystals are anhedral to subhedral in shape, and may reach up to 1.6 mm in length. Some biotite grains are altered to iron-rich biotite (Figs. 6e–f). Ilmenite and ulvöspinel mainly occur as lamellae in magnetite grains (Fig. 6b). Ilmenite also forms typically  $\leq 0.3$  mm individual anhedral grains that are associated with magnetite.

## 4.2. Syenites

Syenites (Fig. 7a) are medium- to coarse-grained, grey, and are composed of microcline (80-90%), plagioclase (3-5%), quartz (2-3%), clinopyroxene (1-3%), magnetite (1-2%), biotite (1%) and apatite (1%). Accessory phases include ilmenite, pyrite and chalcopyrite. The rock appears highly strained and recrystallized, mostly along microcline grain margins due to metamorphism (Figs. 7b–d). Microcline occurs as anhedral, up to 8 mm in length, perthitic grains with a weak to strong preferred orientation (Figs. 7b–c). Crystals display cross-hatched twins and, in general, embayment at the grain boundaries. Potassium feldspar crystals are partially sericitized and host inclusions of magnetite and apatite.

Albite phenocrysts, up to 8 mm in size, are commonly anhedral to subhedral with straight to curved grain outlines, and display undulose extinction (Fig. 7d). Plagioclase microcrystals and quartz with rare K-feldspar crystals, typically  $\leq 0.1$  mm in size, make up the fine-grained recrystallized groundmass (Fig. 7e). In the groundmass, quartz is less abundant than plagioclase. Quartz occurs as anhedral grains that show undulose extinction, commonly embayed crystal boundaries and rare inclusions of plagioclase and potassium feldspar. Quartz also fills micro-veinlets that traverse microcline or albite phenocrysts (Fig. 7d).

Mafic phases are smaller in size relative to K-feldspar crystals. Clinopyroxene occurs mainly as subhedral to euhedral grains up to 1.7 mm in length, most of which are isolated and

preferentially oriented (Fig. 7c). These grains are usually interstitial between felsic minerals and rarely occur as inclusions in alkali feldspar megacrysts. The mineral commonly exhibits sharp and straight to smoothly curved grain boundaries with other minerals and is sometimes partially altered to anhedral amphibole, chlorite and/or biotite (Figs. 7f–h).

Biotite is present as fine-grained (< 0.5 mm in length), subhedral, pleochroic green to brownish flakes partly altered to chlorite (Fig. 7f). These flakes appear as interstitial isolated crystals with random orientation and rarely cluster to form aggregates. Biotite often overgrows or partly replaces clinopyroxene (Figs. 7f and 7i). It commonly shows straight to curved grain boundaries. All these replacement textures can be ascribed to local manifestations of a metamorphic overprint.

Magnetite and ilmenite form decussate aggregates, often slightly elongated, that are oriented approximately in the same direction as K-feldspar or pyroxene (Fig. 7j). They also occur as individual grains within the rock matrix. Crystals are subhedral to euhedral in shape and may reach up to 0.3 mm and 0.5 mm in length for magnetite and ilmenite, respectively. Apatite (0.02 to 0.4 mm in length) forms tiny hexagonal, rounded or rectangular grains that usually occur as inclusions in alkali feldspar, magnetite and pyroxene, or sometimes as isolated crystals. Pyrite and chalcopyrite were observed within the groundmass of the syenites or as inclusions in pyroxene.

## **5. Geochemistry**

### **5.1. Mineral chemistry**

#### **5.1.1. Magnetite**

Electron microprobe analyses of magnetite in the Bikoula BIF show that the magnetite has total iron content (expressed as FeO<sub>t</sub>) between 92.06 and 93.98 % (Table 1). In contrast to

magnetite from typical BIFs found in other regions worldwide (Dupuis and Beaudoin, 2011), it has high  $\text{Al}_2\text{O}_3$  (0.18 to 0.59 %, average 0.34 %) and  $\text{TiO}_2$  (0.09 to 0.56 %, average 0.21 %). In syenites (Appendix A.1), magnetite shows  $\text{FeO}_t$  content as high as in BIF (average 92.99 %), but is highly depleted in all the other elements.

### 5.1.2. Clinopyroxene

Clinopyroxene in syenites is diopsidic in composition ( $\sim\text{Wo}_{40-42}\text{En}_{27-28}\text{Fs}_{19-22}$ ) with minor aegirine and jadeite component ( $\sim 3.4\text{--}8.7$  and  $\sim 0\text{--}4.3$  mol.%, respectively) and has  $X_{\text{Fe}}$  ( $\text{Fe}^{2+}/\text{Mg}+\text{Fe}^{2+}$ ) of  $\sim 0.41\text{--}0.45$  (Fig. 8a, Appendix A.2). Clinopyroxene in the BIF is more iron rich and reaches less calcic and sodic compositions (Appendix B.1, Fig. 8a). The composition ranges from diopside ( $\sim\text{Wo}_{43}\text{En}_{28}\text{Fs}_{29}$ ) to augite ( $\sim\text{Wo}_{37}\text{En}_{26}\text{Fs}_{22}$ ) and with lower aegirine and jadeite contents ( $\sim 3.6\text{--}7.1$  and  $\sim 0\text{--}1.2$  mol.%, respectively) and more  $\text{FeO}_t$  ( $X_{\text{Fe}} \sim 0.46 - 0.51$ ) compared to the clinopyroxene in syenites.

### 5.1.3. Orthopyroxene

Orthopyroxene electron probe microanalyses are tabulated in Appendix B.2. Compared to the clinopyroxenes, the orthopyroxene is more iron-rich ( $\text{Wo}_{1.2-1.6}\text{En}_{34-36}\text{Fs}_{59-62}$ ) (Fig. 8a) with significant concentrations of CaO and MnO (0.58 – 0.75 % and 1.23 – 1.55 %, respectively). Orthopyroxene grains have low  $\text{Al}_2\text{O}_3$  and  $\text{Cr}_2\text{O}_3$  contents ( $< 0.19$  %) and high  $X_{\text{Fe}}$  ( $> 0.6$ ).

### 5.1.4. Amphibole

The calculation of crystal formula for amphiboles shows the following characteristics:  $(\text{Ca}+\text{Na})_{\text{B}} = 1.597\text{--}1.789$  ( $\geq 1$ );  $\text{Ca}_{\text{B}} = 1.597\text{--}1.789$  ( $\geq 1.5$ );  $\text{Si} = 6.341\text{--}6.470$ ;  $\text{Ti} = 0.112\text{--}0.137$  ( $< 0.5$ );  $(\text{Na}+\text{K})_{\text{A}} = 0.910\text{--}0.999$  ( $\geq 0.5$ ) and  $\text{Mg\#} = 0.455\text{--}0.471$  (Appendix B.3). According to



the international nomenclature of amphiboles (Leake et al., 1997), it classifies as ferro-pargasite (Fig. 8b), a member of the calcic group of amphiboles.

#### **5.1.5. Feldspar**

Feldspar in the syenites (Appendices A.3 and A.4) is dominated by perthitic microcline (orthoclase > 96 %) exsolving albite (An = 5.4–8.6 %). Feldspar in the BIF is a plagioclase of oligoclase composition (An = 17.0–19.7 %) and relatively homogeneous in chemical composition (Appendix B.4).

#### **5.1.6. Biotite**

In the BIF, biotite is characterized by  $X_{\text{Fe}} = 0.452\text{--}0.487$ ,  $\text{Al}^{\text{IV}} = 1.076\text{--}1.120$ ,  $\text{Mg\#} = 0.513\text{--}0.548$  and  $\text{Ti} = 0.216\text{--}0.256$  (Appendix B.5). Alteration-type biotite shows higher iron contents and is depleted in  $\text{TiO}_2$ .

#### **5.1.7. Ilmenite**

Major element analyses for ilmenite show  $\text{TiO}_2$  of 50.17 – 51.32 % in syenites and of 51.06 – 52.05 % in BIF (Appendices A.5 and B.6). Ilmenite in BIF has lower  $\text{FeO}_t$  than ilmenite in syenites (average 40.88 % compared to 43.83 %, respectively), while average MnO is higher (7.02 % in BIF compared to 4.38 % in syenites).

### **5.2. Bulk rock geochemistry**

#### **5.2.1. BIF**

Major and trace element data of the BIF samples are listed in Table 2. The  $\text{Fe}_2\text{O}_3$  content varies from 42.79 to 57.89 wt.% (average 49.97 wt.%),  $\text{SiO}_2$  32.3 to 42 wt.% (average 37.77 wt.%) and  $\text{Al}_2\text{O}_3$  0.76 to 7.52 wt.% (average 2.88 wt.%) (Table 2). The contents of other major oxides are also quite significant, i.e. CaO 1.95 – 4.90 wt.%,  $\text{K}_2\text{O}$  0.13 – 1.96 wt.%,  $\text{Na}_2\text{O}$  0.19

– 2.05 wt.% and MgO 3.78 – 5.59 wt.%. The BIF is also characterized by low contents of TiO<sub>2</sub> (0.11 – 0.88 wt.%), MnO (0.39 – 0.56 wt.%) and P<sub>2</sub>O<sub>5</sub> (0.09 – 0.13 wt.%).

Variations in some transition elements are as follows; V 7.58 – 49.56 ppm, Cr 8 – 225.67 ppm, Ni 5.05 – 84.63 ppm, Cu 3.07 – 32.27 ppm and Zn 55.32 – 150.71 ppm. Among the High Field Strength Elements (HFSE), Y, Zr and Sc vary from 10.99 – 28.99 ppm, 7.44 – 111.46 ppm and 0.78 – 6.19 ppm, respectively (Table 2). The contents of Large Ion Lithophile Elements (LILE; Rollinson, 1993) Rb, Sr and Ba vary from 5.09 to 153.73 ppm, 21.45 to 210.09 ppm and 16.82 to 200.46 ppm, respectively. Mo abundances are low (< 6 ppm, Table 2) as expected in older BIFs (Stern et al., 2013; Scott et al., 2008).

Samples analyzed from the Bikoula BIF show variable REE contents with  $\Sigma$ REE ranging from 8.90 to 111.54 ppm (Table 2). All the samples are characterized by high LREE relative to HREE (LREE/HREE ranges from 5.06 and 19.69). PAAS-normalized REE-Y patterns (Fig. 9) show depletion of LREE ( $\text{La/Yb}_{\text{PAAS}} < 1$ ) except in one sample (i.e. sample L271), strong positive Y anomalies ( $\text{Y/Y}^*_{\text{PAAS}} = 0.98 – 6.25$ ) and weak negative Ce anomalies ( $\text{Ce/Ce}^*_{\text{PAAS}} = 0.85 – 0.99$ ). Of the twelve BIF samples analyzed, five display strongly positive Eu anomalies ( $\text{Eu/Eu}^*_{\text{PAAS}} = 1.19 – 3.45$ ), another five display slightly negative Eu anomalies (0.58 – 0.86) while two do not show any anomaly (samples L273 and L282).

### 5.2.2. Syenites

Whole-rock compositions of the studied syenites are presented in Table 3. SiO<sub>2</sub> contents range from 58.29 to 65.73 wt.%, Al<sub>2</sub>O<sub>3</sub> 15.29 to 18.91 wt.% and Fe<sub>2</sub>O<sub>3</sub> 1.15 to 7.82 wt.%. K<sub>2</sub>O and Na<sub>2</sub>O contents are relatively high and similar, both varying between 4.83 and 7.07 wt.% (Table 3). There are significant contents of CaO (0.76 – 3.30 wt.%; average 1.59 wt.%) and MgO (0.22 – 1.32 wt.%; average 0.69 wt.%). Other major oxide components are minor in abundance, namely TiO<sub>2</sub> (0.02 – 0.74 wt.%), P<sub>2</sub>O<sub>5</sub> (0.03 – 0.50 wt.%) and MnO (0.02 – 0.13

wt.%). On the total alkali ( $\text{Na}_2\text{O}+\text{K}_2\text{O}$ ) vs. silica diagram (Cox et al., 1979), the syenites plot in the alkaline fields (syenite and nepheline syenite fields, Fig. 10).

## **6. Discussion**

### **6.1. Mineral paragenesis and effects of metamorphism**

The major mineral assemblage of the Bikoula BIF is magnetite-quartz-orthopyroxene-clinopyroxene (see Fig. 5). This mineralogy, which was observed in all samples, is characteristic of iron formations that have undergone granulite-facies metamorphism (Klein, 2005). As mentioned in section 2.1, the Ntem complex experienced multiple phases of deformation and metamorphism. Thus, the two generations of clinopyroxene identified in the BIF (see Figs. 5d–e), the presence of secondary biotite (see Figs. 6e–f), and the retrogressive reaction textures in the cross-cutting syenites likely result from multistage metamorphism with regressive post-peak events.

In general, exsolution lamellae in pyroxene occur in many igneous and metamorphic rocks as the result of slow cooling from the highest equilibration temperature. This unmixing phenomenon is usually a fossil indicator of very high temperature prevailing during crystallization. Exsolution lamellae in ortho- and clinopyroxene are commonly reported in high-grade metamorphosed BIFs, resulting either from contact metamorphism (e.g., Bonnischen, 1969, 1975; Vaniman et al., 1980) or regional metamorphism (e.g., Sandiford and Powell, 1986a; Gole and Klein, 1981; Harley, 1987; Bhattacharya et al., 1990; Fonarev et al., 2006). Outcrop observation, petrographic analysis and bulk rock composition have shown that the Bikoula iron occurrences are typical of sedimentary banded iron formations (BIFs). The assemblages of the Bikoula BIF do not have hornfelsic textures. Rather, existing studies exclusively point to a regional high-grade metamorphism that prevailed during or soon after emplacement of charnockite (Toteu et al., 1994; Tchameni et al., 2000; Pouclet et al., 2007).

Thus, despite the close spatial relationship between the greenstones and charnockitic country rocks (see Figs. 1 and 2), the metamorphic assemblages in the Bikoula BIF are most likely not the result of contact metamorphism. The peak of the regional metamorphism was constrained at  $750\text{ }^{\circ}\text{C} \pm 50\text{ }^{\circ}\text{C}$  and 5 – 6 Kb (Tchameni, 1997). Therefore, exsolution textures in the Bikoula BIF may likely result from a regional granulite-facies metamorphism affecting the greenstones and magmatic rocks of the Ntem complex.

In the currently observable assemblage, magnetite is the dominant Fe-rich mineral of the Bikoula BIF. Due to the high metamorphic degree and the recrystallized habit of the magnetite crystals, it is not possible to precisely link the evolution of this mineral to the primary process of iron precipitation from seawater. As proposed in many models for BIF formation, the primary iron mineral that precipitated directly from seawater was most likely a  $\text{Fe}^{3+}$  oxyhydroxide, a mixed valence Fe-silicate or a  $\text{Fe}^{2+}$ -carbonate (e.g., ferrihydrite, greenalite, and siderite) (Fischer and Knoll, 2009). Studies of low grade metamorphosed BIF indicates that such primary minerals commonly transform through a large variety of possible abiotic or microbially mediated process into magnetite, hematite, iron carbonates (siderite and ankerite), and various iron-silicate phases (Posth et al., 2013; Smith et al., 2013; Bontognali et al., 2013). Therefore, the magnetite present in the Bikoula BIF may be a recrystallized diagenetic product or, alternatively, it may have formed during a later metamorphic process during which one of the abovementioned primary or diagenetic phase (e.g., siderite, ankerite, Fe-silicate) was transformed into magnetite.

Fukada et al. (2001) proposed that Ti in magnetite from the Superior-type BIF in the Hamersley basin may have originated from hydrothermal solutions, while Ti in silicates was introduced from terrigenous sources. Such explanation for the origin of Ti may also apply to the Bikoula BIF. Ti may have reacted with magnetite during metamorphism to form a Ti-bearing magnetite. Depending on the oxygen fugacity during the cooling process that followed

the peak of metamorphism, some Ti-rich magnetite grains may have been oxidized to ilmenite lamellae while the un-oxidized portions exolved ulvöspinel (Simmons et al., 1974).

Quartz occurs as inclusions in pyroxene, suggesting that it was a phase that crystallized early. Quartz in iron formations is regarded as resulting from recrystallization of initial amorphous silica precipitate (i.e., chert) during metamorphism (Klein, 2005). In the Bikoula BIF, textural analysis revealed that quartz was most likely dynamically recrystallized through bulging, subgrain rotation and grain boundary migration, suggesting its crystallization during prograde metamorphism (Passchier and Trouw, 2005).

Metamorphic Al-bearing phases in the Bikoula BIF comprise of ferro-pargasite, bitotite and oligoclase. Oligoclase inclusions in ferro-pargasite suggest that the latter crystallized after plagioclase. Ferro-pargasite is considered as the product of the reaction between Al-rich clastic material in the BIF and a Ca-Mg-Fe bearing silicate precursor during prograde metamorphism (Wang et al., 2014).

Banding in iron formations may exist on a range of scales: macrobands (meter thick rock types), mesobands (centimeter in thickness) and microbands (millimeter to sub-millimeter) (Trendall and Blockley, 1970). Explanations for banding in BIF include microbial blooms (Trendall and Blockley, 1970), silica precipitation interrupted by pulses of Fe-rich waters (Hamade et al., 2003), density flow deposition (Lascelles, 2007), temperature fluctuation in the oceanic photic zone (Posth et al., 2008), internal dynamics of the geochemical system (Wang et al., 2009), and episodic re-sedimentation of Fe-silicates alternating with periods of non-deposition (Rasmussen et al., 2013). Due to the extensive recrystallization that occurred during metamorphism, it would be too speculative to propose any hypothesis regarding the origin of banding in the Bikoula BIF. In the studied core, it is even difficult to conclude whether some

of the laminations correspond to primary sedimentary layers or represent a banding of purely metamorphic origin.

## **6.2. Detrital input into BIF**

Banded iron formations have long been considered as chemically precipitated sediments. However, many authors agree that, in several cases, precipitation and accumulation of chemical sediments was influenced by the simultaneous deposition of detrital components (Arora et al., 1995; Horstmann and Hålbich, 1995; Basta et al., 2011; Kato et al., 1996; Bolhar et al., 2005b; Sunder Raju, 2009). Elevated  $\text{Al}_2\text{O}_3$  and  $\text{TiO}_2$  are considered as indicators of detrital influx during BIF deposition. Similarly, Si, Mg, Ca and K are thought to be commonly present in detrital sediments (Hatton and Davidson, 2004). Thus, the relatively high abundance of  $\text{Al}_2\text{O}_3$  (0.76 – 7.52 wt.%),  $\text{TiO}_2$  (0.11 – 0.88 wt.%), MgO (3.78 – 5.59 wt.%), CaO (1.95 – 4.90 wt.%),  $\text{K}_2\text{O}$  (0.13 – 1.96 wt.%) and  $\text{Na}_2\text{O}$  (0.19 – 2.05 wt.%) suggest detrital influx during deposition of the Bikoula BIF. Furthermore,  $\text{Al}_2\text{O}_3$  and  $\text{TiO}_2$  vary sympathetically, with a correlation coefficient  $R^2 = 0.34$  (see Table 4), suggesting incorporation of detrital components to the chemical precipitate (González et al., 2009; Pecoits et al., 2009; Lan et al., 2014). Clastic contamination of the Bikoula BIF is further supported by a plot of  $\text{Y}/\text{P}_2\text{O}_5$  as a function  $\text{Zr}/\text{Cr}$  (Marchig et al., 1982). On this diagram, the samples plot either in the deep-sea sediment field or between the latter and the hydrothermal field (Fig. 11).

Trace elements such as Zr, Hf, Y, Rb and Sr are commonly derived from weathering of crustal felsic rocks, whereas Cr, Ni, Co, V and Sc commonly have a mafic source (Rao and Naqvi, 1995). Table 4 displays significant positive correlations of  $\text{Al}_2\text{O}_3$  with LILEs, HFSEs and transition metals. The correlation coefficients ( $R^2$ ) are:  $\text{Al}_2\text{O}_3$  vs. V ( $R^2 = 0.50$ ), vs. Ni (0.39), vs. Zn (0.42), vs. Sc (0.44), vs. Y (0.41), vs. Zr (0.53), vs. Th (0.65), vs. U (0.58), vs. Pb (0.97), vs. Rb (0.73), vs. Sr (0.41) and vs. Ba (0.46) (Table 4). All these relationships may

indicate involvement of clastic materials and further suggest that this detritus might have been derived from weathering of both felsic and mafic (bimodal) sources.

The Th/U ratio can also be used to trace the sources of contaminants in BIF. Possible syn-depositional contaminants of iron formations include volcanic ash, sedimentary detritus and material of uncertain origin such as phosphate grains (Thurstons et al., 2012). Phosphate contamination is generally associated to a Th/U > 5 (Thurstons et al., 2012), while other contaminants (i.e. clastic or volcanic) have Th/U ratios of ca. 3 – 5 (Condie, 1993; Thurstons et al., 2012). Thus, the incorporation of phosphates in iron formation raises the Th/U ratio. In the Bikoula BIF samples, the Th/U ratio lies between 2.93 and 6.92 (average 4.44), indicating little or no phosphate contamination. Zr contents vary sympathetically with the Th/U ratios ( $R^2 = 0.61$ , Table 4), consistently with clastic contamination.

### **6.3. Sources of chemical components**

Several discrimination diagrams have been used by many workers to constrain the influence of seawater, hydrothermal, biogenic and detrital sources on BIF genesis (e.g., Wonder et al., 1988; Stern et al., 2013; Xu et al., 2014). On the Fe-Mn-Al diagram (Bonatti et al., 1979), the Bikoula BIF samples fall in the hydrothermal field (Fig. 12). Similarly, the Al<sub>2</sub>O<sub>3</sub>-SiO<sub>2</sub> discrimination diagram (Wonder et al., 1988) shows that most of the BIF samples plot in the hydrothermal field (Fig. 13). This may indicate that Si and Fe were likely derived from hydrothermal sources. However, two samples plot in the hydrogenous field (Fig. 13), suggesting chemical precipitation from seawater with insignificant hydrothermal input. The seawater input is also suggested by the low CaO/(CaO+MgO) ratios ranging from 0.31 to 0.53 (Table 2), indicative of sediments that precipitated from seawater (Dasgupta et al., 1999).

Bostrom (1973) described a method for assessing dilution by clastic or volcanic detritus of hydrothermal/hydrogenous input and proposed a plot of Fe/Ti versus Al/(Al+Fe+Mn) to

quantify the hydrothermal input relative to the detrital component. Aluminum and titanium cannot be introduced in solution (Ewers and Morris, 1981) and are immobile during hydrothermal, diagenetic and weathering processes (Kato et al., 1996). These two elements can thus be used as proxies to quantify clastic input. Fe and Mn are enriched in components of hydrothermal fluids (Gurvich, 2006), and therefore serve as hydrothermal proxies. Pure hydrothermal sediments are characterized by high Fe/Ti ratio ( $> 7000$ ) while pure clastic sediments are enriched in Al resulting in  $Al/(Al+Fe+Mn) > 0.6$  (Peter and Goodfellow, 1996; Hatton and Davidson, 2004). On the  $Al/(Al+Fe+Mn)$  diagram of Bostrom (1973), the Bikoula BIF samples plot within or close to the field of hydrothermal Soldier Cap Group iron formations (Hatton and Davidson, 2004) and far from the region occupied by modern pelagic-terrigenous sediments (Fig. 14). Figure 14 also suggests quite significant contribution of hydrothermal processes (over 70 vol.%) to the deposition of the Bikoula BIF.

Positive correlations between  $Al_2O_3$  or  $TiO_2$  versus  $Na_2O$ ,  $K_2O$ ,  $MgO$  and  $CaO$  (see Table 4) suggest a common origin for these elements, which were likely present in detrital particles.

Measurements of rare earth elements (REE) in BIFs have often been used to infer the chemical evolution of early oceans and, in particular, to detect the influx of submarine hydrothermal emanations within the basin-waters from where BIFs were precipitated (Derry and Jacobsen, 1990; Bau and Möller, 1993; Kato et al., 1998). Indeed, REE are only minimally fractionated during adsorption onto ferric iron oxyhydroxides precipitates (Bekker et al., 2014) and, due to closed-system conditions for the REE and low fluid/rock ratios, the REE distribution is usually not affected in BIFs that have undergone low- to high-grade regional or contact metamorphism (Bau, 1993). Petrographic analyses suggest that the Bikoula BIF samples studied have experienced high-grade metamorphism with only minor infiltration metasomatism and, therefore, may record quite original REE signals. PAAS-normalized REE-Y patterns (Fig.



9) show that some BIF samples have preserved seawater-like features such as LREE depletion, and positive La and Y anomalies (Alibo and Nozaki, 1999; Bolhar et al., 2004), which points to precipitation from seawater.

Positive Eu anomalies in BIFs have been interpreted as evidence that submarine hydrothermal fluids –that may be source not only of the REE but also of Fe and Si– were important component of the solution from where the Fe-minerals were precipitated (Derry and Jacobsen, 1990; Slack et al., 2007). In the Bikoula BIF, five samples display positive Eu anomalies ( $\text{Eu}/\text{Eu}^*_{\text{PAAS}} = 1.19 - 3.45$ ), pointing to fluxes of high-temperature ( $> 350^\circ\text{C}$ ) hydrothermal fluids. However, seven samples display no or weakly negative Eu anomalies (Fig. 9). The negative Eu anomaly (rarely seen in BIFs) suggests that REE patterns in the Bikoula BIF were also influenced by the heterogeneous input of clastic materials within the depositional basin (Arora et al., 1995; Manikyamba et al., 1993; Manikyamba and Naqvi, 1997b).

Dymek and Klein (1988) and subsequently Alexander et al. (2008) introduced conservative two component mixing diagrams to assess the proportions of seawater and high- $T$  hydrothermal fluids. According to the Sm/Yb-Eu/Sm and Y/Ho-Eu/Sm diagrams (Figs. 15a and b, respectively), extremely small amounts of submarine high- $T$  hydrothermal fluids ( $< 0.1\%$ ) were enough to cause positive Eu anomalies in the Bikoula BIF. Therefore, as observed in other BIFs, it can be deduced that relatively small inputs of high- $T$  hydrothermal fluids may have been sufficient to account for REE-Y distribution in the Bikoula BIF.

#### **6.4. Redox state of ocean water at the time of the Bikoula BIF deposition**

Ce concentrations in BIFs provide information helpful for constraining paleoredox conditions of ancient seawater. In general, modern oxygenated marine settings show a strong negative Ce anomaly when normalized to shale compositions. This arises from the oxidation of  $\text{Ce}^{3+}$  to  $\text{Ce}^{4+}$  and incorporation into Fe-Mn oxyhydroxides, clay particles and organic matter

(Byrne and Sholkovitz, 1996). In contrast, suboxic and anoxic marine waters lack large Ce anomalies as a result of reductive dissolution of the Fe-Mn particles (German et al., 1991). However, it can be challenging to identify Ce anomalies because of anomalous abundances of La. Bau and Dulski (1996) proposed a discrimination diagram that compares  $(\text{Ce}/\text{Ce}^*)_{\text{SN}}$  calculated as  $\text{Ce}_{\text{SN}}/(0.5\text{La}_{\text{SN}} + 0.5\text{Pr}_{\text{SN}})$  to  $(\text{Pr}/\text{Pr}^*)_{\text{SN}}$  calculated as  $\text{Pr}_{\text{SN}}/(0.5\text{Ce}_{\text{SN}} + 0.5\text{Nd}_{\text{SN}})$  to identify ‘‘real’’ La and Ce anomalies in BIFs. As it is the case with other Archean and early Paleoproterozoic BIFs (Planavsky et al., 2010), the Bikoula BIF samples lack negative Ce anomalies (Fig. 16). The lack of evidence for Ce oxidation (implying that the reservoir of  $\text{Fe}^{2+}$  is not fully oxidized) is consistent and supports the commonly held view that, during the Mesoarchean, oceans were (at least partly) anoxic or suboxic, allowing for the transport and accumulation of  $\text{Fe}^{2+}$  (Lyon et al., 2014). Under these conditions, various mechanisms may have caused the progressive mineralization of the  $\text{Fe}^{2+}$  reservoir, leading to the formation of the Bikoula BIF, including: oxidation with  $\text{O}_2$  produced by photosynthetic microbes or oxidation through abiotic photochemical reactions (Cairns-Smith, 1978), microbial oxidation through anoxygenic photosynthesis (Widdel et al., 1993), or even through direct precipitation from anoxic seawater as ferrous or mixed valences minerals (e.g., siderite, iron-rich clay minerals) (Rasmussen et al., 2014).

## Conclusion

The Bikoula BIF is located within the Mesoarchean Ntem complex, South Cameroon, and it is included in a ~3.1 Ga greenstone belt hosted by charnockitic granites. The BIF sequence is locally cross-cut by late syenitic veins.

Petrographic analysis revealed that the BIF mainly consists of magnetite, quartz, orthopyroxene and clinopyroxene. BIF suffered high-grade metamorphism that caused intense recrystallization of precursor precipitates. The presence of minor amounts of Al-rich phases

(ferro-pargasite, biotite and oligoclase) and high contents of Al<sub>2</sub>O<sub>3</sub>, TiO<sub>2</sub>, Na<sub>2</sub>O, K<sub>2</sub>O, MgO and CaO suggest that the primary chemical precipitate was contaminated by a significant amount of clastic material.

REE-Y patterns of the Bikoula BIF display positive Eu anomaly, which indicates that seawater from which the BIF precipitated was influenced by hydrothermal solutions. In some samples, Eu anomalies are very low or even slightly negative, likely as the result of variable amount of clastic contamination. Finally, the lack of Ce anomalies in the studied BIF suggests that its deposition occurred in a basin that was not fully oxic (i.e., at least partly anoxic or suboxic), where it was possible to transport and concentrate dissolved Fe<sup>2+</sup>.

## **Acknowledgments**

This paper is an integral part of the first author's Ph.D thesis at the University of Yaoundé 1 (Cameroon). The authors thank Aluvance Plc for permission to sample diamond drill core from the Bikoula Iron Ore Project, and providing technical data on the project. Much thanks to its VP Operations, Jonathan Hunt, for assistance during field work. Daniela Hunziker and Lukas Martin are gratefully acknowledged for invaluable assistance in microprobe analysis. We also thank Remy Luechinger for the preparation of polished thin sections, and the two anonymous reviewers for constructive comments that helped to improve an earlier manuscript version. This project was financially supported by the Swiss Government Excellence Scholarships and the Department of Earth Sciences of ETH Zurich. J.V. acknowledges the ERC starting grant (335577) of L. Tajcmanova for financial support.

## **References**

543 Alexander, B.W., Bau, M., Andersson, P., Dulski, P., 2008. Continentally-derived solutes in  
 544 shallow Archean seawater: rare earth element and Nd isotope evidence in iron formation from  
 545 the 2.9 Ga Pongola Supergroup, South Africa. *Geochim. Cosmochim. Acta* 72, 378–394.

546 Alibo, D.S., Nozaki, Y., 1999. Rare earth elements in seawater: particle association, shale-  
 547 normalization, and Ce oxidation. *Geochim. Cosmochim. Acta* 63, 363–372.

548 Aluvance Plc, 2014. <http://aluvance.com/> (Accessed 15 October 2014).

549 Anderson, K.F.E., Wall, F., Rollinson, G.K., Moon, C.J., 2014. Quantitative mineralogical and  
 550 chemical assessment of the Nkout iron ore deposit, Southern Cameroon. *Ore Geol. Rev.* 62,  
 551 25–39.

552 Arora, M., Govil, P., Charan, S., Uday Raj, B., Balaram, V., Manikyamba, C., Chatterjee, A.,  
 553 Naqvi, S., 1995. Geochemistry and origin of Archaean banded iron formation from Bababudan  
 554 Belt, India. *Econ. Geol.* 90, 2040–2057.

555 Basta, F.F., Maurice, A.E., Fontbote, L., Favarger, P.-Y., 2011. Petrology and geochemistry of  
 556 the banded iron formation (BIF) of Wadi Karim and Um Anab, Eastern Desert, Egypt:  
 557 implications for the origin of Neoproterozoic BIF. *Prec. Res.* 187, 277–292.

558 Bau, M., 1993. Effects of syn- and post-depositional processes on the rare-earth element  
 559 distribution in Precambrian Iron-formations. *Eur. J. Mineral.* 5, 257–267.

560 Bau, M., Dulski, P., 1996. Distribution of yttrium and rare-earth elements in the Penge and  
 561 Kuruman iron-formations, Transvaal Supergroup, South Africa. *Prec. Res.* 79, 37–55.

562 Bau, M., Dulski, P., 1999. Comparing yttrium and rare earths in hydrothermal fluids from the  
 563 Mid-Atlantic Ridge: implications for Y and REE behaviour during near-vent mixing and for  
 564 the Y/Ho ratio of Proterozoic seawater. *Chem. Geol.* 155, 77–90.

565 Bau, M., Möller, P., 1993. Rare earth element systematics of the chemically precipitated  
 566 component in early Precambrian iron formations and the evolution of the terrestrial  
 567 atmosphere–hydrosphere–lithosphere system. *Geochim. Cosmochim. Acta* 57, 2239–2249.

568 Bekker, A., Planavsky, N.J., Krapez, B., Rasmussen, B., Hofman, A., Slack, J.F., Rouxel, O.J.,  
 569 Konhauser, K.O., 2014. Iron Formations: Their Origins and Implications for Ancient Seawater  
 570 Chemistry. In Mackenzie, F.T. (volume ed.), *Sediments, Diagenesis and Sedimentary Rocks*  
 571 (*Treatise on Geochemistry*), Amsterdam: Elsevier, pp. 561–628.

572 Bhattacharya, A., Spiering, B., Sen, S.K., Natarajan, R., Mazumdar, A.C., 1990. Compositional  
 573 characteristics and phase equilibria in manganiferous iron formations from a high-grade terrain  
 574 near Satnuru, Karnataka, India. *J. Metam. Geol.* 8, 525–538.

575 Bolhar, R., Kamber, B.S., Moorbath, S., Fedo, C.M., Whitehouse, M.J., 2004. Characterisation  
 576 of early Archaean chemical sediments by trace element signatures. *Earth Planet. Sci. Lett.* 222,  
 577 43–60.

578 Bolhar, R., Van Kranendonk, M.J., Kamber, B.S., 2005b. A trace element study of siderite–  
 579 jasper banded iron formation in the 3.45 Ga Warrawoona Group, Pilbara Craton—Formation  
 580 from hydrothermal fluids and shallow seawater. *Prec. Res.* 137, 93–114.

581 Bonatti, E., Kolla, V., Moore, W.S., Stern, C., 1979. Metallogenesis in marginal basins: Fe-rich  
 582 basal deposits from the Philippine Sea. *Marine Geology* 32, 21–37.

583 Bonnichsen, B., 1969. Metamorphic pyroxenes and amphiboles in the Biwabik iron formation,  
 584 Dunka River area, Minnesota. *Mineral. Soc. Amer. Spec. Pap.* 2, 217–239.

585 Bonnischen, B., 1975. Geology of the Biwabik iron formation, Dunka River area, Minnesota.  
 586 *Econ. Geol.* 70, 319–340.

587 Bontognali, T.R.R., Fischer, W.W., Föllmi, K.B., 2013. Siliciclastic associated banded iron  
588 formation from the 3.2 Ga Moodies Group, Barberton Greenstone Belt, South Africa. *Prec. Res.*  
589 226, 116–124.

590 Bostrom, K., 1973. The origin and fate of ferromanganoan active ridge sediments. Stockholm  
591 *Contribution of Geology* 27, 149–243.

592 Byrne, R.H., Sholkovitz, E.R., 1996. Marine chemistry and geochemistry of the lanthanides, in  
593 Gschneidner, K.A., Jr., and Eyring, L., eds., *Handbook on the physics and chemistry of the rare*  
594 *earths*, Volume 23: Amsterdam, Elsevier Ltd., p. 497–593.

595 Cairns-Smith, A.G., 1978. Precambrian solution photochemistry, inverse segregation, and  
596 banded iron formations. *Nature* 276, 807–808.

597 Chombong, N.N., Suh, C.E., Ilouga, D.C.I., 2013. New detrital zircon U-Pb ages from BIF-  
598 related metasediments in the Ntem Complex (Congo craton) of southern Cameroon, West  
599 Africa. *Natural Sciences* 5 (7), 835–847.

600 Cloud, P., 1968. Atmospheric and hydrospheric evolution on the primitive Earth. *Science* 160,  
601 729–736.

602 Condie, K.C., 1993. Chemical composition and evolution of the upper continental crust;  
603 contrasting results from surface samples and shales. *Chem. Geol.* 104, 1–37.

604 Cox, K.G., Bell, J.D., Pankhurst, R.J., 1979. *The Interpretation of Igneous Rocks*. George Allen  
605 & Unwin, London, United Kingdom, 445 pp.

606 Craig, J.R., Vokes, F.M., 1993. The metamorphism of pyrite and pyritic ores: an overview.  
607 *Mineralogical Magazine* 57, 3–18.

608 Dasgupta, H.C., Sambasiva Rao, V.V., Krishna, C., 1999. Chemical environments of deposition  
609 of ancient iron- and manganese-rich sediments and cherts. *Sediment. Geol.* 125, 83–98.

610 Derry, L.A., Jacobsen, S.B., 1990. The chemical evolution of Precambrian seawater: Evidence  
611 from REEs in banded iron formations. *Geochem. Cosmochim. Acta* 54, 2965–2977.

612 Dymek, R.F., Klein, C., 1988. Chemistry, petrology and origin of banded iron-formation  
613 lithologies from the 3800 Ma Isua supracrustal belt, West Greenland. *Prec. Res.* 39, 247–302.

614 Ewers, W.E., Morris R.C., 1981. Studies of the Dales Gorge Member of the Brockman Iron  
615 Formation, Western Australia. *Econ. Geol.* 76, 1929–1953.

616 Fischer, W.W., Knoll, A.H., 2009. An iron shuttle for deep-water silica in Late Archean and  
617 Early Paleoproterozoic iron formation. *Geological Society of America Bulletin* 121, 222–235.

618 Fonarev, V.I., Pilugin, S.M., Savko, K.A., Novikova, M.A., 2006. Exsolution textures of  
619 orthopyroxene and clinopyroxene in high-grade BIF of the Voronezh Crystalline Massif:  
620 evidence of ultrahigh-temperature metamorphism. *J. Metam. Geol.* 24, 135–151.

621 Fukuda, K., Matsunaga, M., Kato, Y., Nakai, I., 2001. Chemical speciation of trace titanium in  
622 Hamersley banded iron formations by X-ray fluorescence imaging and xanes analysis. *J. Trace*  
623 *Microprobe Tech.* 19, 509–519.

624 Ganno, S., Ngnotue T., Kouankap Nono, G.D., Nzenti, J.P., Notsa, F.M., 2015. Petrology and  
625 geochemistry of the banded iron-formations from Ntem complex greenstones belt, Elom area,  
626 Southern Cameroon: Implications for the origin and depositional environment. *Chem. Erde* 75,  
627 375–387.

628 Ganno, S., Moudioh, C., Nchare, N.A., Kouankap Nono, G.D., Nzenti, J.P., 2016. Geochemical  
 629 Fingerprint and Iron Ore Potential of the Siliceous Itabirite from Palaeoproterozoic Nyong  
 630 Series, Zambi Area, Southwestern Cameroon. *Resource Geology* 66, No. 1, 71–80.

631 German, C.R., Holliday, B.P., Elderfield, H., 1991. Redox cycling of rare earth elements in the  
 632 suboxic zone of the Black Sea. *Geochim. Cosmochim. Acta* 55, 3553–3558.

633 Gole, M.J., Klein, C., 1981. High-grade metamorphic Archean banded iron-formations,  
 634 Western Australia: assemblages with coexisting pyroxenes  $\pm$  fayalite. *Am. Mineral.* 66, 87–99.

635 González, P.D., Sato, A.M., Llambías, E.J., Petronilho, L.A., 2009. Petrology and geo-  
 636 chemistry of the banded iron formation in the Eastern Sierras Pampeanas of San Luis  
 637 (Argentina): implications for the evolution of the Nogolí Metamorphic Complex. *J. S. Am.*  
 638 *Earth Sci.* 28, 89–112.

639 Gross, G.A., 1980. A classification of iron formations based on depositional environments.  
 640 *Canadian Mineralogist* 18, 215–222.

641 Gurvich, E.G., 2006. *Metalliferous Sediments of the World Ocean: Fundamental Theory of*  
 642 *Deep-Sea Hydrothermal Sedimentation*. Springer Berlin, 416p.

643 Hamade, T., Konhauser, K.O., Raiswell, R., Goldsmith, S., Morris, R.C., 2003. Using Ge/Si  
 644 ratio to decouple iron and silica fluxes in Precambrian banded iron formations. *Geology* 31,  
 645 35–38.

646 Harley, S.L., 1987. A pyroxene-bearing meta-ironstone and other pyroxene granulites from  
 647 Tonagh Island, Enderby Land, Antarctica: further evidence for very high temperature ( $> 980^{\circ}\text{C}$ )  
 648 Archean regional metamorphism in the Napier Complex. *Journal of Metamorphic Geology* 5,  
 649 341–356.



650 Hatton, O., Davidson, G., 2004. Soldiers Cap Group iron-formations, Mt. Isa Inlier, Australia,  
651 as windows into the hydrothermal evolution of a base-metal-bearing Proterozoic rift basin.  
652 Australian J. Earth Sci. 51, 85–106.

653 Holland, H.D., 1973. The oceans: a possible source of iron in iron formations. Econ. Geol. 68,  
654 1169–1172.

655 Horstmann, U.E., Hälbig, I.W., 1995. Chemical composition of banded iron formations of the  
656 Griqualand West Sequence, Northern Cape Province, South Africa, in comparison with other  
657 Precambrian iron formations. Prec. Res. 72, 109–145.

658 Ilouga, D.C.I., Suh C.E., Ghogomu, R.T., 2013. Textures and Rare Earth Elements  
659 Composition of Banded Iron Formations (BIF) at Njweng Prospect, Mbalam Iron Ore District,  
660 Southern Cameroon. International Journal of Geosciences 4, 146–165.

661 James, H.L., 1954. Sedimentary facies of iron-formation. Econ. Geol. 49, 235–293.

662 Kato, Y., Kawakami, T., Kano, T., Kunugiza, K., Swamy, N.S., 1996. Rare-earth element  
663 geochemistry of banded iron formations and associated amphibolite from the Sargur belts, south  
664 India. J. Southeast Asian Earth Sci. 14, 161–164.

665 Kato, Y., Ohta, I., Tsunematsu, T., Watanabe, Y., Isozaki, Y., Maruyama, S., Imai, N., 1998.  
666 Rare earth element variations in mid-Archean banded iron formations: implications for the  
667 chemistry of ocean and continent and plate tectonics. Geochim. Cosmochim. Acta 62, 3475–  
668 3497.

669 Klein, C., 2005. Some Precambrian banded iron-formations (BIFs) from around the world: their  
670 age, geologic setting, mineralogy, metamorphism, geochemistry, and origins. Am. Mineral. 90,  
671 1473–1499.

672 Konhauser, K.O., Pecoits, E., Lalonde, S.V., Papineau, D., Nisbet, E.G., Barley, M.E., Arndt,  
 673 N.T., Zahnle, K., Kamber, B.S., 2009. Oceanic nickel depletion and a methanogen famine  
 674 before the great oxidation event. *Nature* 458, 750–753.

675 Lan, T.G., Fan, H.R., Santosh, M., Hu, F.F., Yang, K.F., Yang, Y.H., Liu, Y.S., 2014. U–Pb  
 676 zircon chronology, geochemistry and isotopes of the Changyi banded iron formation in eastern  
 677 Shandong Province: constraints on BIF genesis and implications for Paleoproterozoic tectonic  
 678 evolution of the North China Craton. *Ore Geol. Rev.* 56, 472–486.

679 Lascelles, D.F., 2007. Black smokers and density currents: an uniformitarian model for the  
 680 genesis of banded iron-formations. *Ore Geol. Rev.* 32, 381–411.

681 Leake, B.E., Woolley, A.R., Arps, C.E.S., Birch, W.D., Gilbert, M.C., Grice, J.D., Hawthorne,  
 682 F.C., Kato, A., Kisch, H.J., Krivovichev, V.G., Linthout, K., Laird, J., Mandarino, J., Maresch,  
 683 W.V., Nickel, E.H., Rock, N.M.S., Schumacher, J.C., Smith, D.C., Stephenson, N.C.N.,  
 684 Ungaretti, L., Whittaker, E.J.W., Guo, Y.Z., 1997. Nomenclature of amphiboles: report of the  
 685 subcommittee on amphiboles of the International Mineralogical Association, Commission on  
 686 New Minerals and Mineral Names. *Eur. J. Mineral.* 9, 623–651.

687 Lerouge, C., Cocherie, A., Toteu, S.F., Milesi, J.P., Penaye, J., Tchameni, R., Nsifa, N.E.,  
 688 Fanning, C.M., 2006. SHRIMP U–Pb zircon dating for the Nyong Series, South West  
 689 Cameroon. *J. Afri. Earth Sci.* 44, 413–427.

690 Lyons, T.W., Reinhard, C.T., Planavsky, N.J., 2014. The rise of oxygen in Earth’s early ocean  
 691 and atmosphere. *Nature* 506, 307–315.

692 Manikyamba, C., Balaram, V., Naqvi, S.M., 1993. Geochemical signatures of polygenetic  
 693 origin of a banded iron formation (BIF) of the Archaean Sandur greenstone belt (schist belt)  
 694 Karnataka nucleus, India. *Prec. Res.* 61, 137–164.

695 Manikyamba, C., Naqvi, S.M., 1997b. Mineralogy and geochemistry of Archaean greenstone  
696 belt-hosted Mn formations and deposits of the Dharwar Craton: redox potential of proto-oceans.  
697 Geological Society Special Publication No. 119, 91–103.

698 Marchig, V., Gundlach, H., Möller, P., Schley, F., 1982. Some geochemical indicators for  
699 discrimination between diagenetic and hydrothermal metalliferous sediments. *Mar. Geol.* 50,  
700 241–256.

701 Maurizot, P., Abessolo, A., Feybesse, J.L., Johan Lecomte, P., 1986. Etude de prospection  
702 minière du Sud-Ouest Cameroun : Synthèse des travaux de 1978 à 1985. Rapp. BRGM. 85,  
703 CMR 066.

704 Morimoto, N., Fabries, J., Ferguson, A.K., Ginzburg, I.V., Ross, M., Seifert, F.A., Zussman, J.,  
705 Aoki, K., Gottardi, G., 1989. Nomenclature of pyroxenes. *Can. Mineral.* 27, 143–156.

706 Morris, R.C., Horwitz, R.C., 1983. The origin of the iron-formation-rich Hamersley Group of  
707 Western Australia–Deposition on a platform. *Prec. Res.* 21, 273–297.

708 Nédélec, A., Macaudière, J., Nzenti, J.P., Barbey, P., 1986. Evolution structurale et  
709 métamorphique des schistes de Mbalmayo (Cameroun): implications pour la structure de la  
710 zone mobile panafricaine d’Afrique centrale au contact du craton du Congo. *C. R. Acad. Sci.*,  
711 Paris, Tome 303 (Série II 1), 75–80.

712 Nforba, M.T., Kabeyene, V.K., Suh, C.E., 2011. Regolith Geochemistry and Mineralogy of the  
713 Mbalam Itabirite-Hosted Iron Ore District, South Eastern Cameroon. *Open Journal of Geology*  
714 1, 17–36.

715 Nzenti, J.P., Barbey, P., Macaudière, J., Soba, D., 1988. Origin and evolution of the late  
716 Precambrian high grade Yaoundé gneisses (Cameroon). *Prec. Res.* 38, 91–109.

717 Passchier, C.W., Trouw, R.A.J., 2005. *Microtectonics*, second ed. Springer Verlag, Berlin,  
718 366p.

719 Pecoits, E., Gingras, M.K., Barley, M.E., Kappler, A., Posth, N.R., Konhauser, K.O., 2009.  
720 Petrography and geochemistry of the Dales Gorge banded iron formation: paragenetic  
721 sequence, source and implications for palaeo-ocean chemistry. *Prec. Res.* 172, 163–187.

722 Peter, J.M., Goodfellow, W.D., 1996. Mineralogy, bulk and rare earth element geochemistry of  
723 massive sulphide-associated hydrothermal sediments of the Brunswick Horizon, Bathurst  
724 Mining Camp, New Brunswick. *Can. J. Earth Sci.* 33, 252–283.

725 Planavsky, N.J., Bekker, A., Rouxel, O.J., Kamber, B.S., Hofmann, A.W., Knudsen, A., Lyons,  
726 T.W., 2010. Rare earth element and yttrium compositions of Archean and paleoproterozoic Fe  
727 formations revisited: new perspectives on the significance and mechanisms of deposition.  
728 *Geochim. Cosmochim. Acta* 74, 6387–6405.

729 Posth, N.R., Hegler, F., Konhauser, K.O., Kappler, A., 2008. Alternating Si and Fe deposition  
730 caused by temperature fluctuations in Precambrian oceans. *Nat. Geosci.* 1, 703–708.

731 Posth, N.R., Köhler, I., Swanner, E.D., Schröder, C., Wellmann, E., Binder, B., Konhauser,  
732 K.O., Neumann, U., Berthold, C., Nowak, M., Kappler, A., 2013. Simulating Precambrian  
733 banded iron formation diagenesis. *Chem. Geol.* 362, 66–73.

734 Pouclet, A., Tchameni, R., Mezger, K., Vidal, M., Nsifa, N.E., Penaye, P., 2007. Archaean  
735 crustal accretion at the northern border of the Congo Craton (South Cameroon). The  
736 charnockite-TTG link. *Bulletin de la Société Géologique de France* 178 (5), 3–14.

737 Rao, T.G., Naqvi, S.M., 1995. Geochemistry, depositional environment and tectonic setting of  
738 the BIF's of the late Archean Chitradurga schist belt, India. *Chem. Geol.* 121, 217–243.

739 Rasmussen, B., Krapez, B., Meier, D.B., 2014. Replacement origin for hematite in 2.5 Ga  
740 banded iron formation: Evidence for postdepositional oxidation of iron-bearing minerals.  
741 Geological Society of America Bulletin 126, 438–446.

742 Rasmussen, B., Meier, D.B., Krapez, B., Muhling, J.R., 2013. Iron silicate microgranules as  
743 precursor sediments to 2.5-billion-year-old banded iron formations. *Geology* 41, 435–438.

744 Robb, L., 2005. *Introduction to Ore-Forming Processes*. Blackwell Publishing, 373p.

745 Robertson, A.H.F., Hudson, J.D., 1973. Cyprus umbers: chemical precipitates on a Tethyan  
746 ocean ridge. *Earth Planet. Sci. Lett.* 18, 93–101.

747 Rollinson, H.R., 1993. *Using Geochemical Data: Evaluation, Presentation, Interpretation*.  
748 Longmann Group UK, 352p.

749 Sandiford, M., Powell, R., 1986a. Pyroxene exsolution in granulites from Fyfe Hills, Enderby  
750 Land, Antarctica: evidence for 1000°C metamorphic temperatures in Archean continental crust.  
751 *American Mineralogist* 71, 946–954.

752 Scott, C., Lyons, T.W., Bekker, A., Shen, Y., Poulton, S.W., Chu, X., Anbar, A.D., 2008.  
753 Tracing the stepwise oxygenation of the Proterozoic ocean. *Nature* 452, 456–459.

754 Shang, C.K., Satir, M., Nsifa, E.N., Liegeois, J.P., Siebel, W., Taubald, H., 2007. Archean  
755 high-K granitoids produced by remelting of the earlier Tonalite–Trondhjemite–Granodiorite  
756 (TTG) in the Sangmelima region of the Ntem complex of the Congo craton, southern  
757 Cameroon. *Int. J. Earth Sci.* 96, 817–842.

758 Shang, C.K., Satir, M., Siebel, W., Nsifa, E.N., Taubald, H., Liegeois, J.P., Tchoua, F.M.,  
759 2004a. TTG magmatism in the Congo craton; a view from major and trace element

760 geochemistry, Rb–Sr and Sm–Nd systematics of TTG magmatism in the Congo craton: case of  
 761 the Sangmelima region, Ntem complex, southern Cameroon. *J. Afri. Earth Sci.* 40, 61–79.

762 Simmons, E.C., Lindsley, D.H., Papike, J.J., 1974. Phase Relations and Crystallization  
 763 Sequence in a Contact-Metamorphosed Rock from the Gunflint Iron Formation, Minnesota. *J.*  
 764 *Petrol.* 15, 539–565.

765 Slack, J.F., Grenne, T., Bekker, A., Rouxel, O.J., and Lindberg, P.A., 2007. Suboxic deep  
 766 seawater in the late Paleoproterozoic: Evidence from hematitic chert and iron formation related  
 767 to seafloor-hydrothermal sulfide deposits, central Arizona, USA. *Earth Planet. Sci. Lett.* 255,  
 768 243–256.

769 Smith, A.J.B., Beukes, N.J., and Gutzmer, J., 2013, The composition and depositional  
 770 environments of Mesoarchean iron formations of the West Rand Group of the Witwatersrand  
 771 Supergroup, South Africa. *Economic Geology and the Bulletin of the Society of Economic*  
 772 *Geologists* 108, 111–134.

773 Stern, R.J., Mukherjee, S.K., Miller, N.R., Ali, K., Johnson, P.R., 2013. ~750 Ma banded iron  
 774 formation from the Arabian-Nubian Shield – Implications for understanding neoproterozoic  
 775 tectonics, volcanism, and climate change. *Prec. Res.* 239, 79–94.

776 Suh, C.E., Cabral, A.R., Ndime, E., 2009. Geology and ore fabrics of the Nkout high-grade  
 777 hematite deposit, southern Cameroon. In: P.J. Williams et al. (editors), *Smart Science for*  
 778 *Exploration and Mining, Proceedings of the Tenth Biennial SGA Meeting of The Society for*  
 779 *Geology Applied to Mineral Deposits*, Townsville, Australia, pp. 558–560.

780 Suh, C.E., Cabral, A.R., Shemang, E.M., Mbinkar, L., Mboudou, G.G.M., 2008. Two  
 781 contrasting iron deposits in the Precambrian mineral belt of Cameroon, West Africa.  
 782 *Exploration and Mining Geology* 17, 197–207.

783 Sunder Raju, P.V., 2009. Petrography and geochemical behaviour of trace element, REE and  
 784 precious metal signatures of sulphidic banded iron formations from the Chikkasiddavanahalli  
 785 area, Chitradurga schist belt, India. *J. Asi. Earth Sci.* 34, 663-673.

786 Takam, T., Arima, M., Kokonyangi, J., Dunkley, D.J., Nsifa, E.N., 2009. Paleoarchaeoan  
 787 charnockites in the Ntem complex, Congo craton, Cameroon: insights from SHRIMP zircon  
 788 U–Pb ages. *Journal of Mineralogical and Petrological Sciences* 104, 1–11.

789 Tchameni, R., 1997. Géochimie et géochronologie des formations de l'Archéen et du  
 790 Paléoproterozoïque du Sud-Cameroun (Groupe du Ntem, Craton du Congo). Thèse de  
 791 l'Université d'Orléans, France, 395p.

792 Tchameni, R., Lerouge, C., Penaye, J., Cocherie, A., Milesi, J.P., Toteu, S.F., Nsifa, E.N., 2010.  
 793 Mineralogical constraint for metamorphic conditions in a shear zone affecting the Archean  
 794 Ngoulemakong tonalite, Congo craton (Southern Cameroon) and retentivity of U–Pb SHRIMP  
 795 zircon dates. *J. Afri. Earth Sci.* 58, 67–80.

796 Tchameni, R., Mezger, K., Nsifa, N.E., Pouclet, A., 2000. Neoarchaeoan evolution in the Congo  
 797 Craton: evidence from K rich granitoids of the Ntem complex, Southern Cameroon. *J. Afri.*  
 798 *Earth Sci.* 30, 133–147.

799 Tchameni, R., Mezger, K., Nsifa, E.N., Pouclet, A., 2001. Crustal origin of Early Proterozoic  
 800 syenites in the Congo craton (Ntem complex), South Cameroon. *Lithos* 57, 23–42.

801 Tchameni, R., Pouclet, A., Mezger, K., Nsifa, E.N., Vicat, J.P., 2004. Monozircon and Sm–Nd  
 802 whole rock ages from the Ebolowa greenstone belts: evidence for the terranes older than 2.9 Ga  
 803 in the Ntem Complex (Congo craton, South Cameroon). *Journal of the Cameroon Academy of*  
 804 *Sciences* 4 (3), 213–224.

805 Thurston, P.C., Kamber, B.S., Whitehouse, M., 2012. Archean cherts in banded iron formation:  
806 insight into Neoarchean ocean chemistry and depositional processes. *Prec. Res.* 214, 227–257.

807 Toteu, S.F., Van Schmus, W.R., Penaye, J., Nyobe, J.B., 1994. U–Pb and Sm–Nd evidence for  
808 Eburnean and Pan-African high grade metamorphism in cratonic rocks of Southern Cameroon.  
809 *Prec. Res.* 67, 321–347.

810 Trendall, A.F., 2002. The significance of iron-formation in the Precambrian stratigraphic  
811 record. *Spec. Publs int. Ass. Sediment.* 33, 33–66.

812 Trendall, A.F., Blockley, J.G., 1970. The iron formations of the Precambrian Hamersley Group  
813 Western Australia with special reference to the crocidolite. Geological Survey of Western  
814 Australia Bulletin, Perth 365 p.

815 Vaniman, D. T., Papike, J. J. & Labotka, T., 1980. Contact metamorphic effect of the Stillwater  
816 Complex, Montana: the concordant iron formation. *American Mineralogist*, 65, 1087–1102.

817 Wang, C.L., Zhang, L.C., Lan, C.Y., Dai, Y.P., 2014. Petrology and geochemistry of the  
818 Wangjiazhuang banded iron formation and associated supracrustal rocks from the Wutai  
819 greenstone belt in the North China Craton: Implications for their origin and tectonic setting.  
820 *Prec. Res.* 255, 603–626.

821 Wang, Y., Xu, H., Merino, E., Konishi, H., 2009. Generation of banded iron formations by  
822 internal dynamics and leaching of oceanic crust. *Nature Geoscience* 2, 781–784.

823 Whitney, D.L., Evans, B.W., 2010. Abbreviations for names of rock-forming minerals.  
824 *American Mineralogist* 95, 185–187.

825 Widdel, F., Schnell, S., Heising, S., Ehrenreich, A., Assmus, B., Schink, B., 1993. Ferrous iron  
826 oxidation by anoxygenic phototrophic bacteria. *Nature* 362, 834–836.



827 Wonder, J., Spry, P., Windom, K., 1988. Geochemistry and origin of manganese-rich rocks  
 828 related to iron-formation and sulfide deposits, western Georgia. *Econ. Geol.* 83 (5), 1070–1081.

829 Xu, D.R., Wang, Z.L., Chen, H.Y., Hollings, P., Jansen, N.H., Zhang, Z.C., Wu, C.J., 2014.  
 830 Petrography and geochemistry of the Shilu Fe–Co–Cu ore district, South China: Implications  
 831 for the origin of a Neoproterozoic BIF system. *Ore Geol. Rev.* 57, 322–350.

832 Zhang, J., Nozaki, Y., 1996. Rare earth elements and yttrium in seawater: ICP-MS  
 833 determinations in the East Caroline, Coral Sea, and South Fiji basins of the western South  
 834 Pacific Ocean. *Geochim. Cosmochim. Acta* 60, 4631–4644.

835

## 836 **Table captions**

837 **Table 1.** Electron microprobe analyses of magnetite from the Bikoula BIF.

838 **Table 2.** Major (wt.%) and trace (ppm) element contents in the Bikoula BIF.

839 **Table 3.** Major element contents (wt.%) in syenites.

840 **Table 4.** Linear inter-element correlations ( $R^2$ ) for all BIF samples ( $n = 12$ ).

841 **Appendix A.** Electron microprobe analyses of minerals in syenites.

842 **A.1.** Magnetite

843 **A.2.** Clinopyroxene

844 **A.3.** Microcline

845 **A.4.** Albite

846 **A.5.** Ilmenite

847 **Appendix B.** Electron microprobe analyses of minerals from the Bikoula BIF.

848 **B.1.** Clinopyroxene

849 **B.2.** Orthopyroxene

850 **B.3.** Ferro-pargasite

851 **B.4.** Oligoclase

852 **B.5.** Biotite

853 **B.6.** Ilmenite

854

855 **Figure captions**

856 **Fig. 1.** Geological map of SW Cameroon (modified after Pouclet et al., 2007). The star indicates  
857 the position where the studied BIF occurs.

858 **Fig. 2.** Geological map showing the location where the core intersecting the studied BIF was  
859 drilled.

860 **Fig. 3.** Field photos of the Bikoula BIF. (a and b) Weathered outcrops of BIF occurring in the  
861 study area. (c) Hand sample collected from an outcrop, showing dark iron-rich bands and light  
862 quartz-rich bands as well as yellowish goethite or limonite resulting from supergene  
863 weathering.

864 **Fig. 4.** Stratigraphy of the Bikoula BIF with sample locations.

865 **Fig. 5.** Core section (a) and photomicrographs (b–e) of the Bikoula BIF, (c) and (d) taken with  
866 crossed polars. (a) Unweathered BIF drill core sample showing black Fe-rich bands alternating  
867 with whitish silica bands and greenish silicate bands. (b) BIF consisting of alternating magnetite

(Mag), quartz (Qtz) and pyroxene (Opx and Cpx) bands. (c) BIF showing magnetite, pyroxene and quartz bands; some quartz grains show preferred orientation and are dynamically recrystallized. (d) BIF showing pyroxene exsolution textures; orthopyroxene (Opx) exsolving clinopyroxene (Cpx) lamellae and first generation of clinopyroxene (Cpx<sup>I</sup>) exsolving Opx lamellae. (e) Photomicrograph showing later generation of clinopyroxene (Cpx<sup>II</sup>) developed in the interstices of large Opx grains. Mineral abbreviations according to Whitney and Evans (2010).

**Fig. 6.** Photomicrographs and SEM image of the Bikoula BIF; red arrows indicate alteration/replacement texture. (a) Reflected light photomicrograph illustrating magnetite band with cracks; pyrite (Py) grains are associated with magnetite. (b) SEM image illustrating interlocking magnetite grains containing ilmenite (Ilm) and ulvöspinel (fine, dark) lamellae. (c) Reflected light photomicrograph of pyrite and magnetite; pyrite replaces magnetite along cracks. (d) Reflected light photomicrograph of pyrite, pyrrhotite (Po) and chalcopyrite (Ccp); pyrrhotite replaces pyrite. (e–f) Cross polarized light photomicrograph of BIF consisting of oligoclase (Olg), ferro-pargasite (Fp), magnetite, biotite (Bt) and iron-rich biotite; iron-rich biotite (Fe-Bt) occurs as alteration phase which replacing ferro-pargasite or biotite as shown with red arrows.

**Fig. 7.** Petrographic characteristics of the syenites intercalated with the BIF, red arrows indicate alteration/replacement textures. (a) Drill core sample showing macroscopic features. (b–c) Syenite consisting of microcline (Mc) and clinopyroxene in a fine recrystallized groundmass; grains show a preferred orientation. (d) Albite (Ab) and microcline phenocrysts surrounded by groundmass; groundmass fills interstices and fractures of phenocrysts. (e) Groundmass consisting of quartz, polysynthetic twinned plagioclase and k-feldspar (Kfs). (f) Photomicrograph showing chlorite (Chl) replacing biotite (left red arrow) and biotite and chlorite replacing clinopyroxene (right red arrow) (Plane polarized light). (g–h) Plane polarized

light (g) and crossed polarized light (h) photomicrographs showing replacement reaction texture of clinopyroxene by amphibole (Amp) and chlorite. (i) Photomicrograph of syenite consisting of microcline, clinopyroxene, biotite and magnetite-ilmenite aggregate; biotite overgrowths clinopyroxene. (j) Magnetite-ilmenite aggregates, preferentially oriented; note some fine rounded apatite grains (Reflected light microscopy).

**Fig. 8.** (a) Compositional ranges of pyroxenes (Morimoto et al., 1989) including clinopyroxene in syenite, clinopyroxene and orthopyroxene in BIF. (b) Amphibole compositions (diamonds) plotted on Si vs. Mg# diagram (Leake et al., 1997).

**Fig. 9.** PAAS-normalized REE-Y patterns of the Bikoula BIF. Seawater data: average of 0, 9 and 30 m depth samples of station SA-5 (Zhang and Nozaki, 1996).

**Fig. 10.** Compositions of the syenites (black diamonds) plotted in a total alkalis vs. silica (TAS) diagram (after Cox et al., 1979).

**Fig. 11.** Compositions of the Bikoula BIF plotted in a bivariate diagram of Y/P<sub>2</sub>O<sub>5</sub> vs. Zr/Cr. Deep-sea, diagenetic and metalliferous fields are based on data from Marchig et al. (1982).

**Fig. 12.** Ternary Fe–Mn–Al plot showing hydrothermal and non-hydrothermal fields for modern marine ferromanganese deposits (Bostrom, 1973). The Bikoula BIF plots within the hydrothermal field. Fields for metalliferous sediments from the East Pacific Rise (EPR) (Bostrom, 1973), Deep Sea Drilling Project (DSDP) Leg 31 (Bonatti et al., 1979), Cyprus umbers (Robertson and Hudson, 1973) and other oceanic sediments are also included.

**Fig. 13.** Plot of Al<sub>2</sub>O<sub>3</sub> vs. SiO<sub>2</sub> (after Wonder et al., 1988) to illustrate the origin of primary chemical precipitates of the Bikoula BIF samples (Filled triangles).

**Fig. 14.** Composition of the Bikoula BIF (Filled triangles) plotted on the Fe/Ti vs. Al/(Al+Fe+Mn) discrimination diagram (after Bostrom, 1973). This diagram is proposed for

estimating the relative contribution from hydrothermal inputs in the fluid from where BIF precipitated. Hydrothermal chemical sediment of the Soldier Cap Group iron formations (Hatton and Davidson, 2004) is plotted to show the hydrothermal input.

**Fig. 15.** Composition of the Bikoula BIF (triangles) plotted in an elemental ratio diagram with two-component conservative mixing lines for Eu/Sm, Sm/Yb, and Y/Ho (after Alexander et al., 2008). The high- $T$  ( $>350^{\circ}\text{C}$ ) hydrothermal fluids follow Bau and Dulski (1999) and the Pacific seawater follow Alibo and Nozaki (1999). (a) Plot of Sm/Yb vs. Eu/Sm showing a  $\leq 0.1\%$  high- $T$  hydrothermal fluid contribution. (b) Plot of Y/Ho vs. Eu/Sm showing a  $\leq 0.1\%$  high- $T$  hydrothermal fluid contribution.

**Fig. 16.** Composition of the Bikoula BIF plotted in a  $(\text{Ce}/\text{Ce}^*)_{\text{SN}}$  vs.  $(\text{Pr}/\text{Pr}^*)_{\text{SN}}$  diagram after Bau and Dulski (1996).

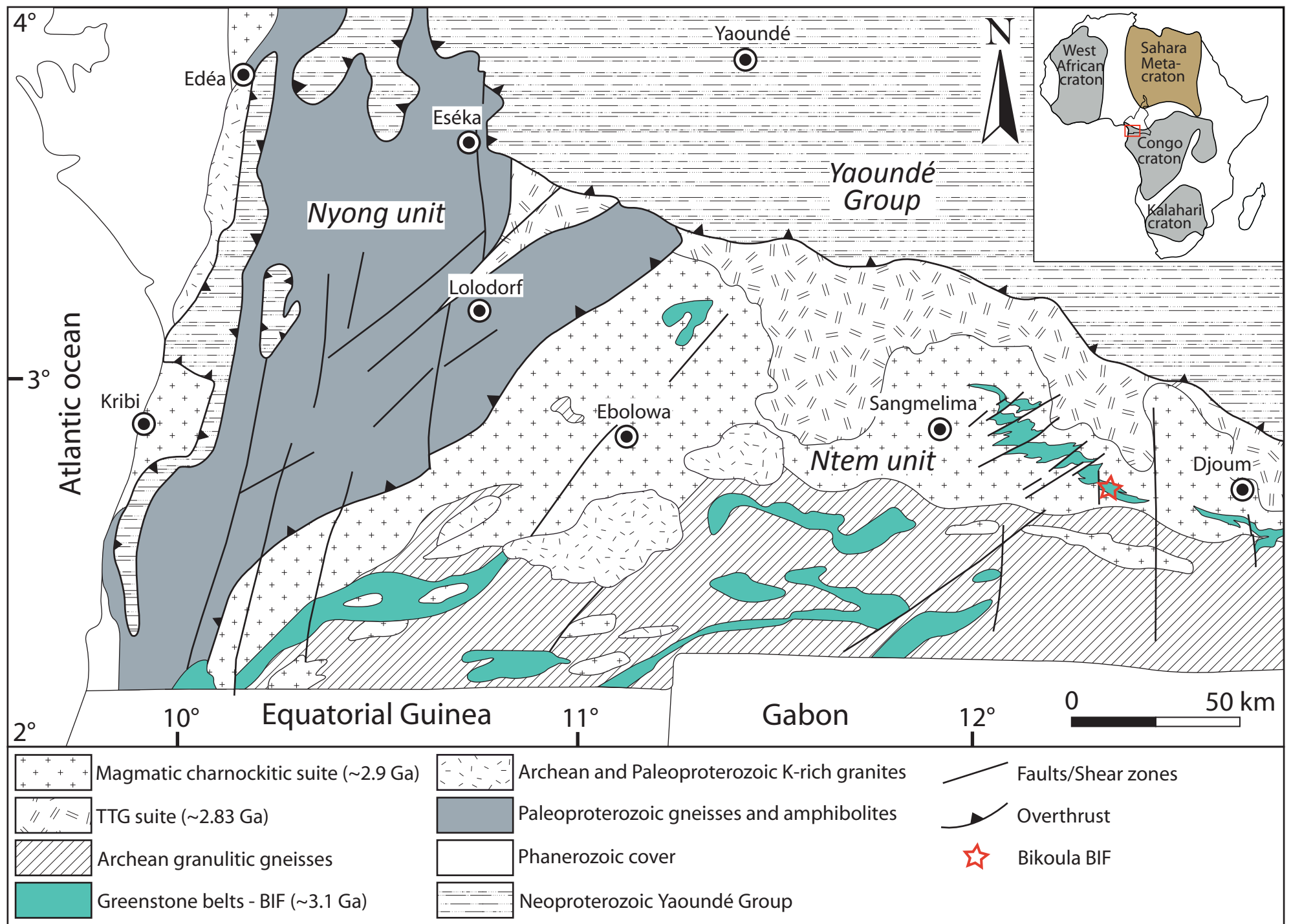


Fig. 1  
(2 columns)

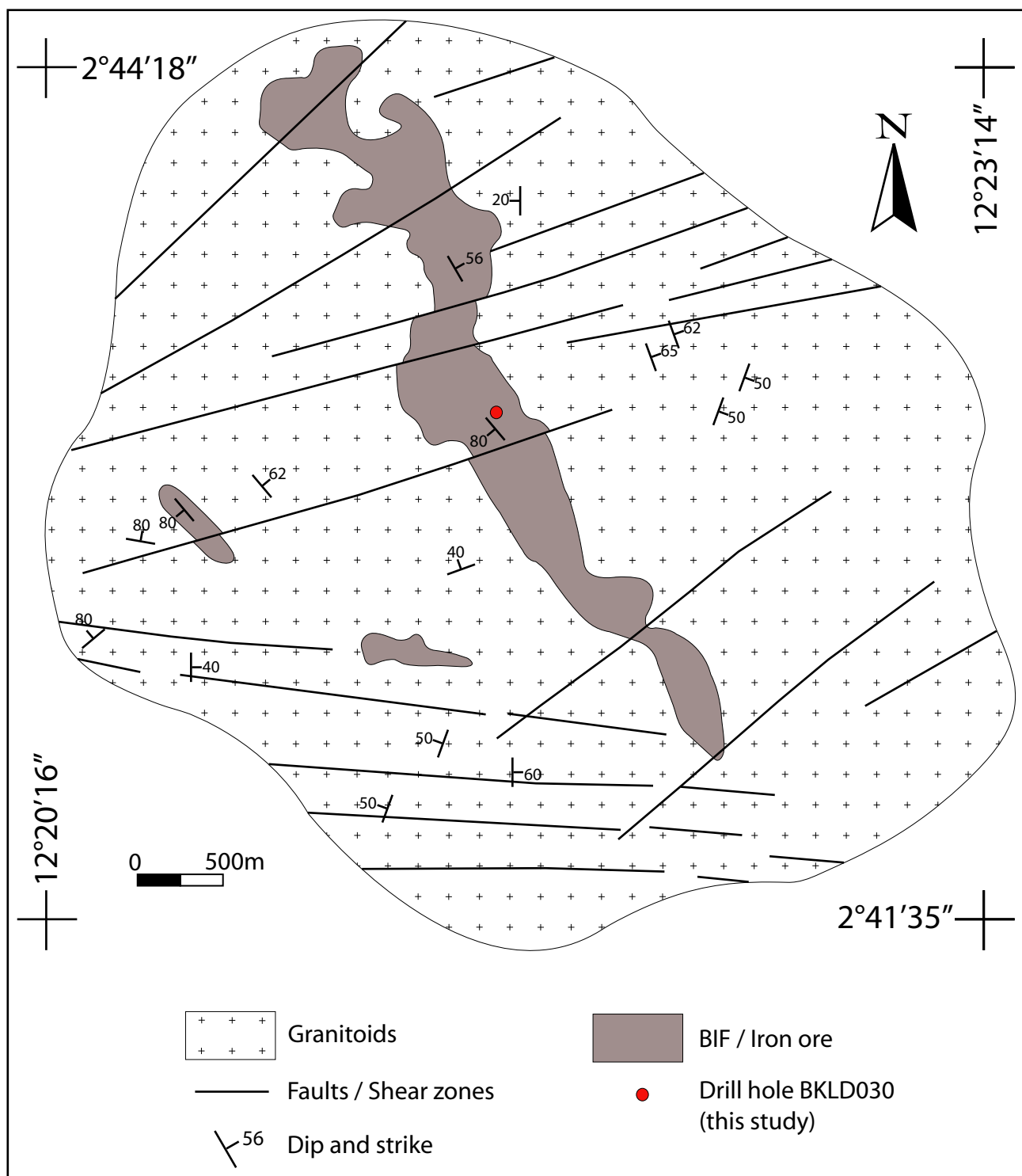


Fig. 2  
(1 column)

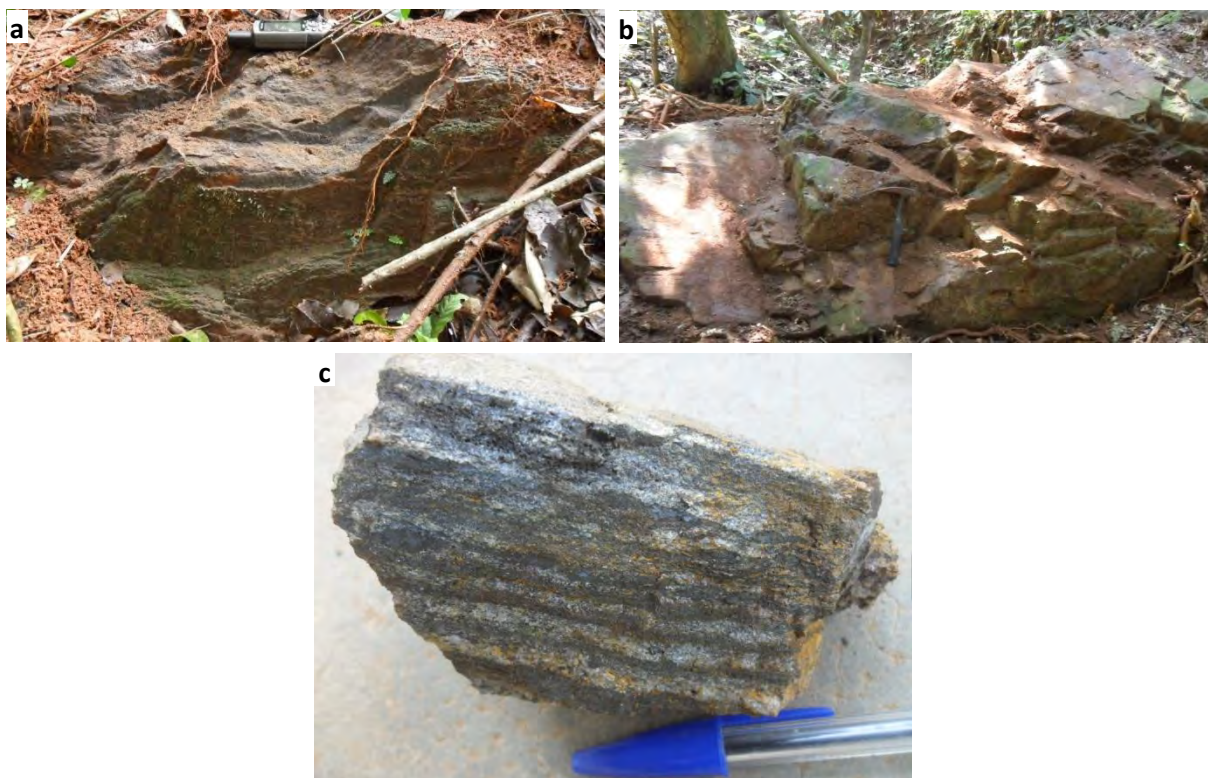


Fig. 3  
(2 columns)



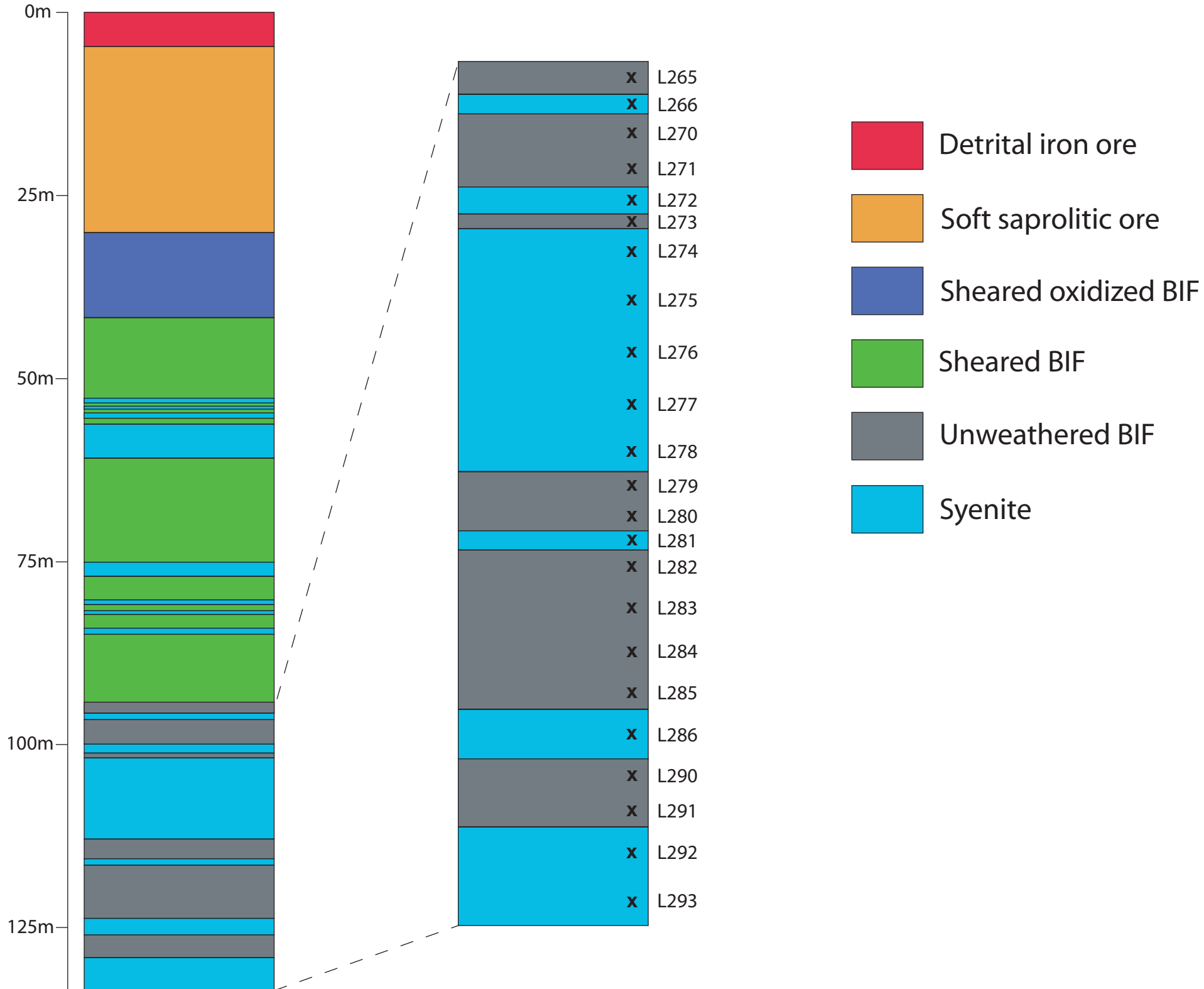


Fig. 4  
(2 columns)

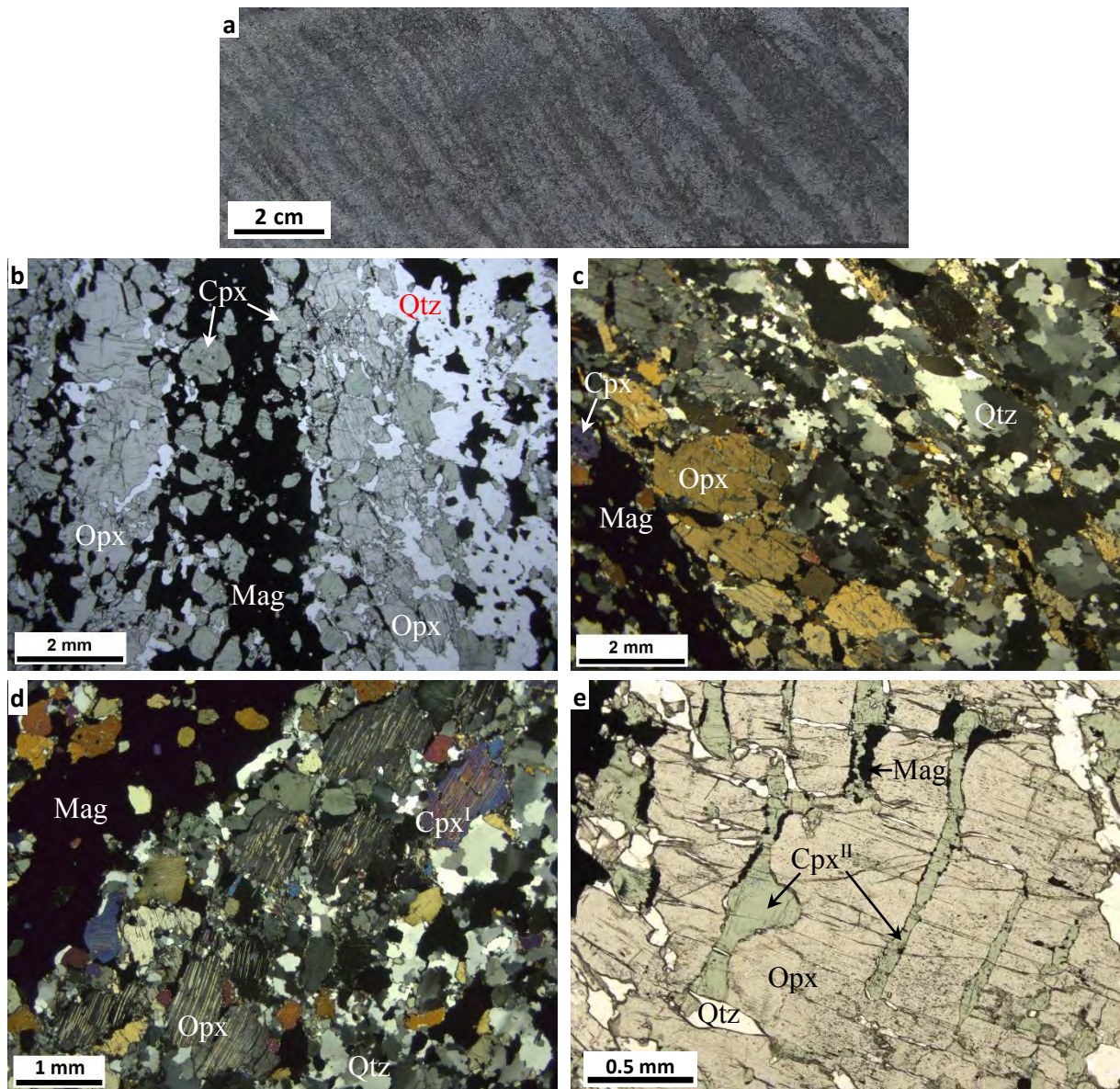


Fig. 5  
(2 columns)



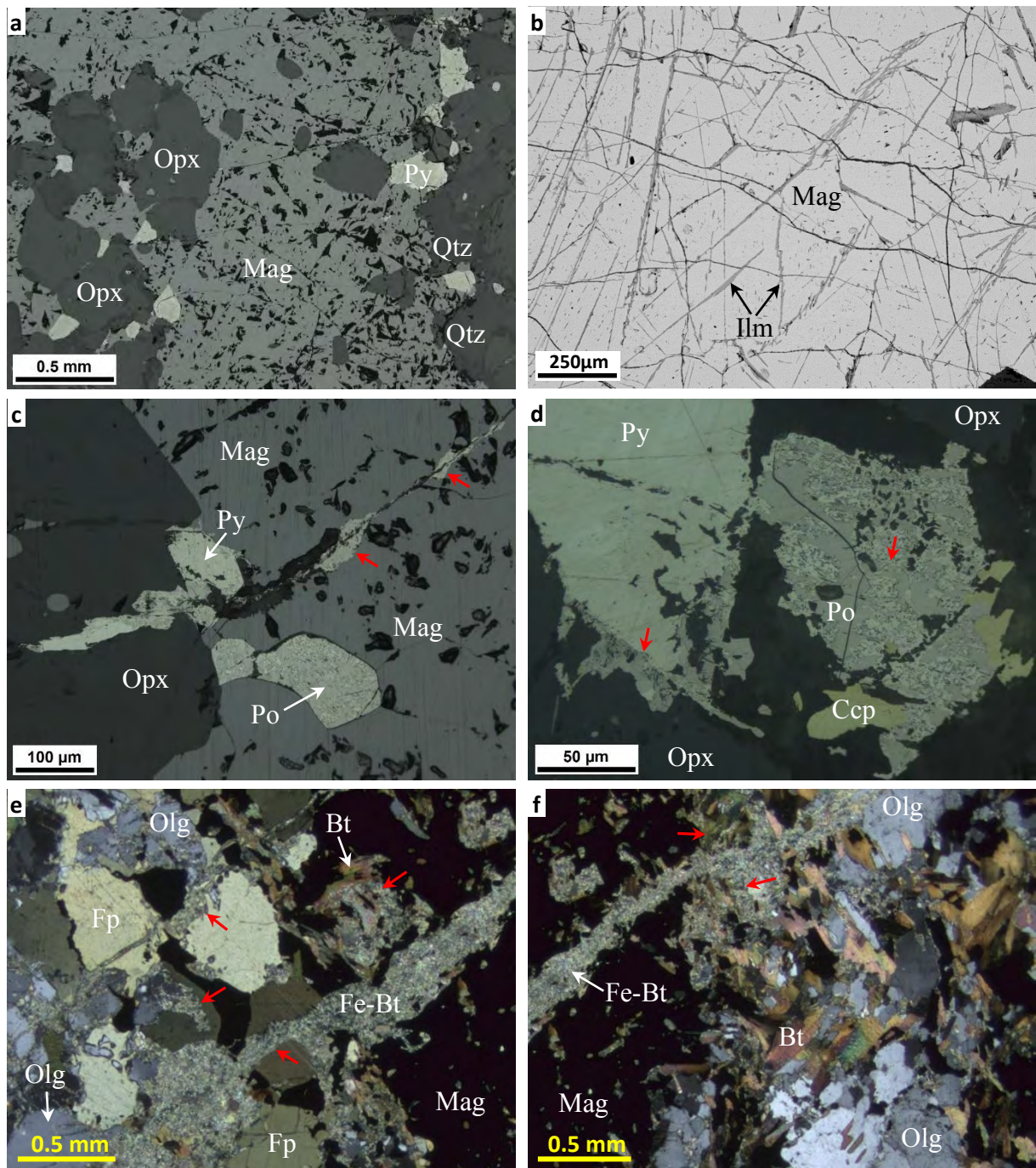


Fig. 6  
(2 columns)



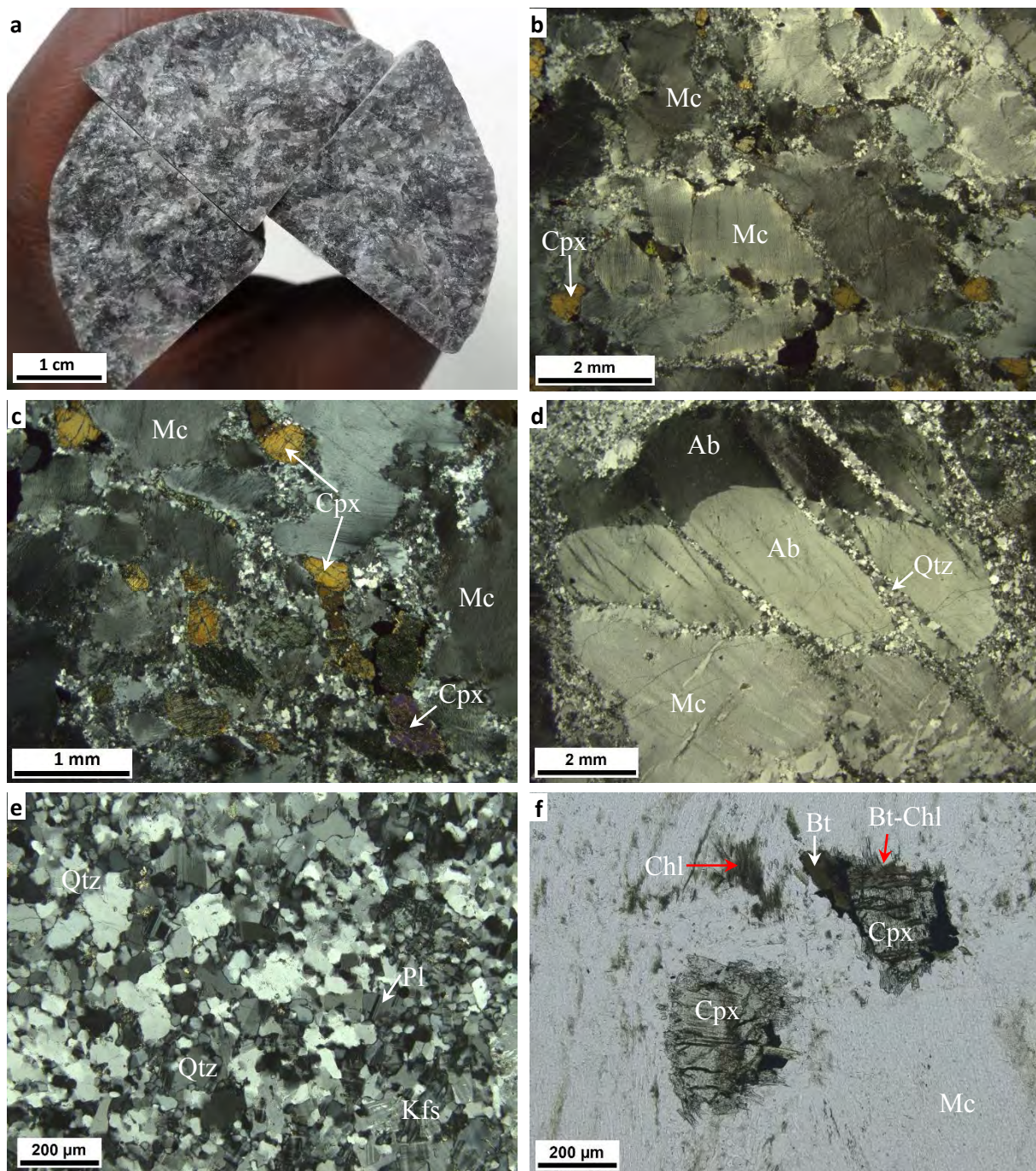


Fig. 7  
(2 columns)



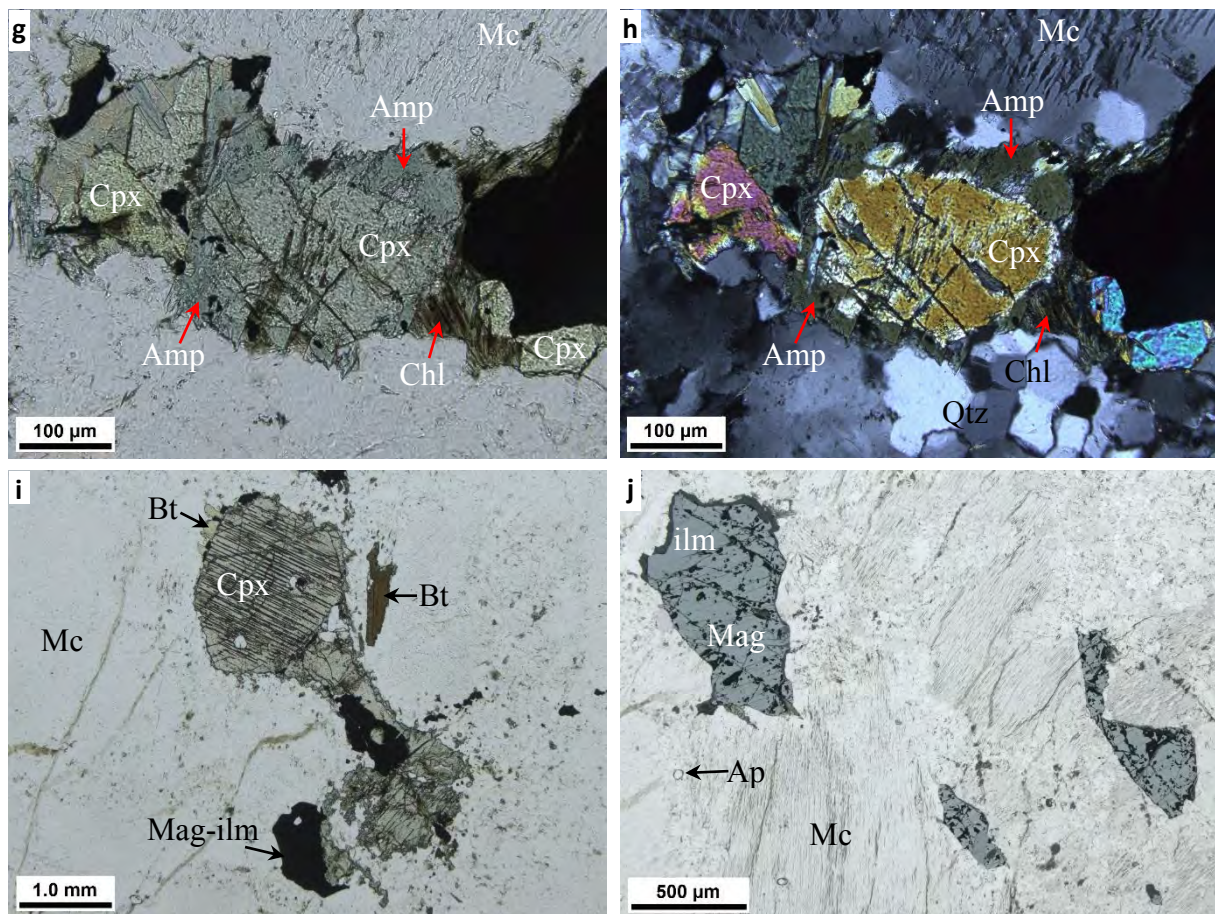


Fig. 7. Continued.

(2 columns)

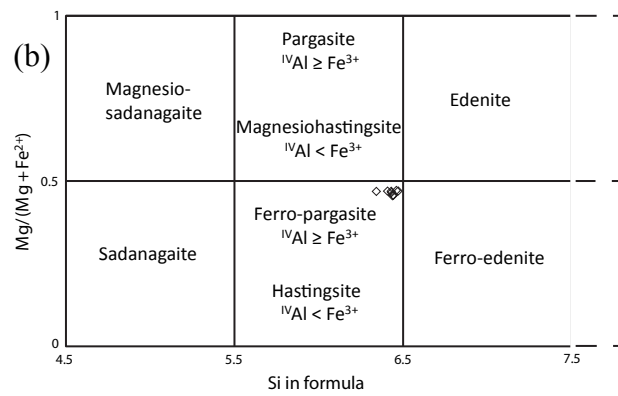
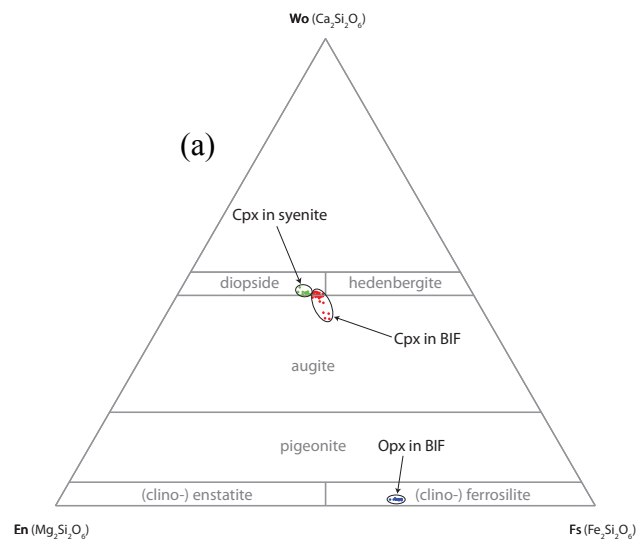


Fig. 8  
(1 column)

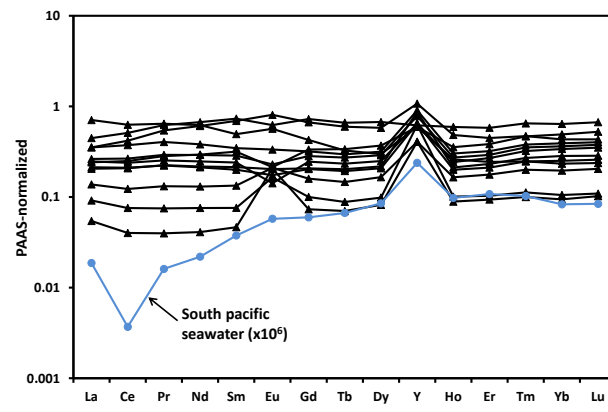


Fig. 9  
(1 column)

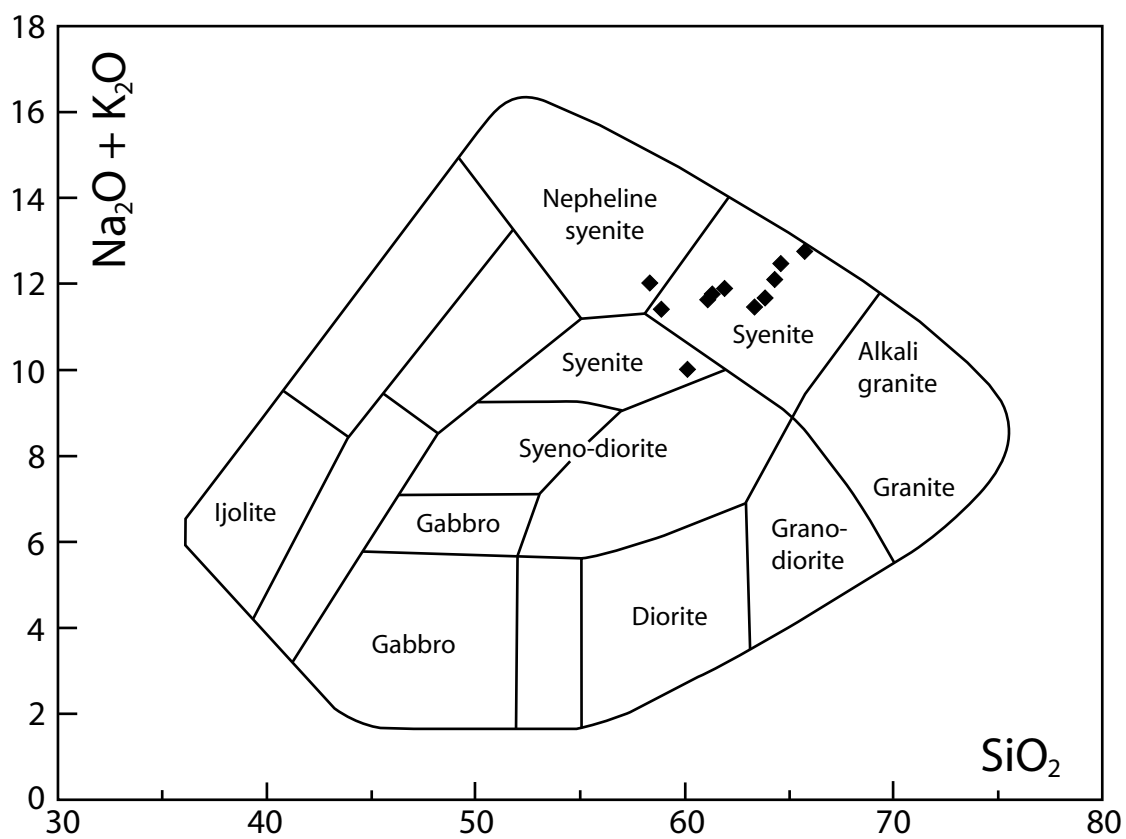


Fig. 10  
(1 column)



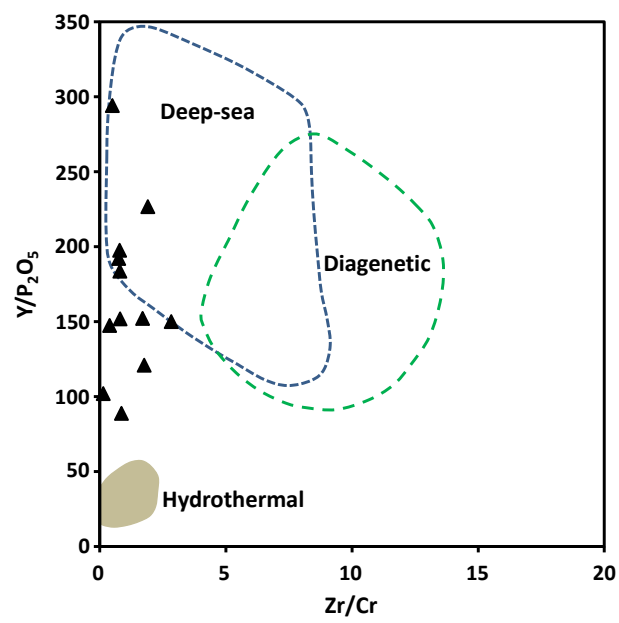


Fig. 11

(1 column)

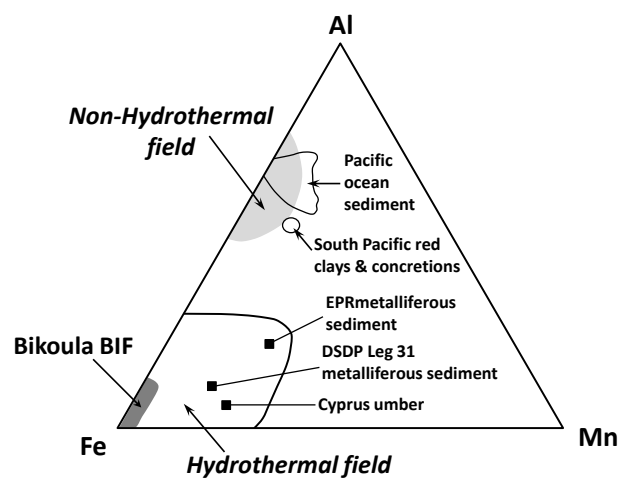


Fig. 12

(1 column)

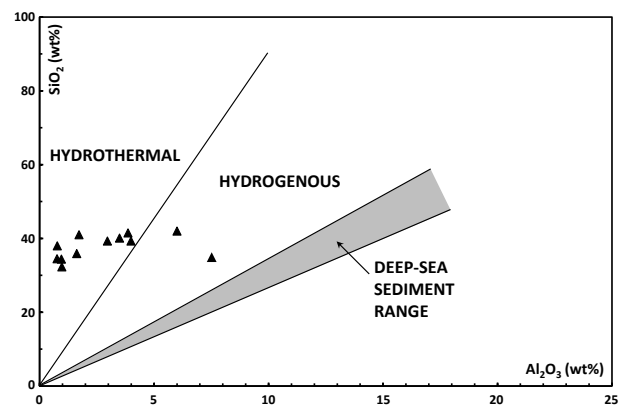


Fig. 13

(1 column)

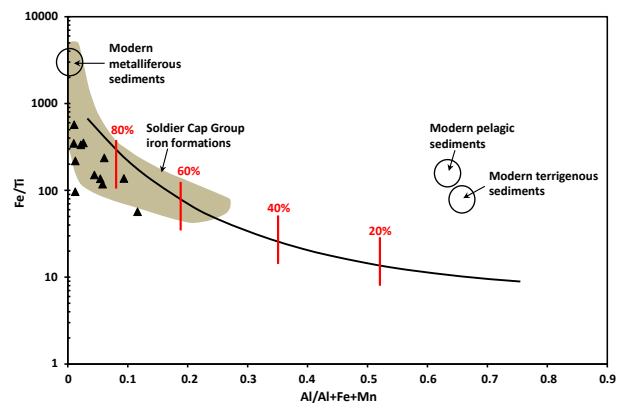


Fig. 14

(1 column)

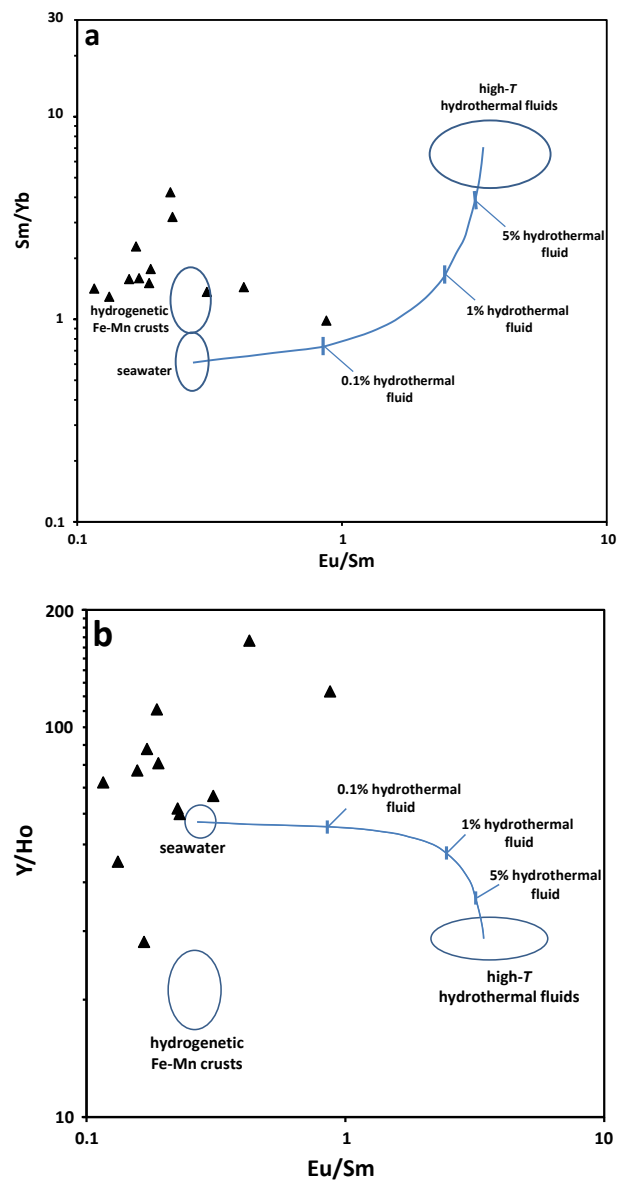


Fig. 15  
(1 column)

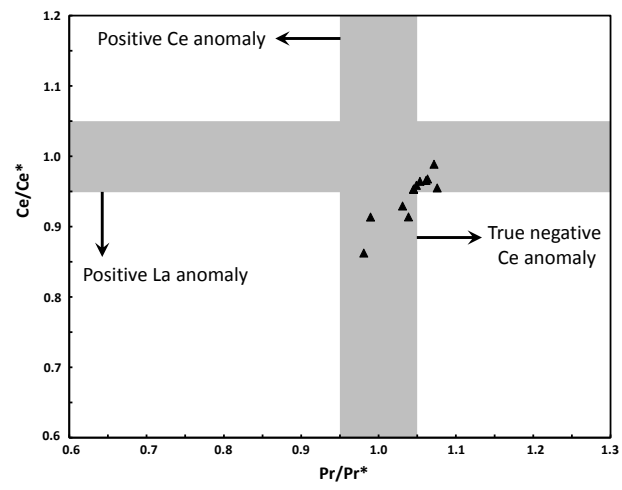


Fig. 16  
(1 column)

**Table 1**

No.	SiO <sub>2</sub>	TiO <sub>2</sub>	Al <sub>2</sub> O <sub>3</sub>	Cr <sub>2</sub> O <sub>3</sub>	FeO <sub>t</sub>	MnO	MgO	CaO	Na <sub>2</sub> O	K <sub>2</sub> O	Total
1	0.07	0.10	0.25	0.00	93.98	0.07	0.02	0.02	0.04	0.01	94.56
2	0.07	0.09	0.25	0.00	93.75	0.07	0.04	0.20	0.00	0.01	94.48
3	0.09	0.11	0.28	0.00	93.45	0.04	0.00	0.16	0.04	0.01	94.18
4	0.06	0.09	0.18	0.00	93.70	0.07	0.00	0.09	0.01	0.00	94.20
5	0.10	0.13	0.35	0.00	93.02	0.07	0.01	0.00	0.05	0.00	93.72
6	0.11	0.10	0.31	0.00	93.09	0.04	0.04	0.02	0.00	0.00	93.72
7	0.12	0.12	0.35	0.00	92.95	0.07	0.01	0.01	0.00	0.00	93.64
8	0.11	0.12	0.37	0.00	92.41	0.03	0.03	0.01	0.00	0.00	93.07
9	0.11	0.13	0.35	0.01	93.14	0.01	0.00	0.01	0.05	0.00	93.81
10	0.10	0.12	0.35	0.00	93.10	0.05	0.01	0.00	0.08	0.02	93.83
11	0.10	0.10	0.31	0.00	93.02	0.06	0.00	0.01	0.00	0.01	93.63
12	0.11	0.11	0.38	0.02	93.13	0.07	0.01	0.02	0.00	0.00	93.86
13	0.12	0.13	0.37	0.04	92.92	0.03	0.00	0.01	0.03	0.00	93.65
14	0.14	0.10	0.31	0.01	93.29	0.05	0.00	0.01	0.03	0.00	93.95
15	0.11	0.09	0.37	0.00	93.25	0.09	0.00	0.00	0.03	0.01	93.95
16	0.07	0.10	0.27	0.01	92.96	0.00	0.03	0.05	0.00	0.00	93.48
17	0.09	0.11	0.59	0.01	92.31	0.04	0.02	0.00	0.00	0.01	93.19
18	0.14	0.21	0.25	0.02	92.45	0.08	0.00	0.00	0.00	0.00	93.16
19	0.13	0.36	0.54	0.01	92.06	0.10	0.02	0.00	0.01	0.00	93.22
20	0.13	0.35	0.47	0.00	92.83	0.09	0.01	0.00	0.00	0.01	93.88
21	0.14	0.45	0.25	0.02	92.54	0.07	0.01	0.01	0.00	0.02	93.51
22	0.10	0.22	0.22	0.00	93.11	0.02	0.02	0.00	0.07	0.00	93.77
23	0.10	0.49	0.22	0.04	92.72	0.12	0.00	0.02	0.01	0.00	93.72
24	0.08	0.48	0.53	0.01	92.66	0.08	0.01	0.01	0.03	0.00	93.90
25	0.09	0.43	0.50	0.00	92.47	0.04	0.02	0.00	0.00	0.00	93.55
26	0.13	0.39	0.40	0.00	93.08	0.10	0.00	0.00	0.00	0.00	94.10
27	0.12	0.25	0.25	0.00	93.16	0.03	0.01	0.02	0.00	0.01	93.85
28	0.14	0.56	0.40	0.00	92.96	0.13	0.02	0.00	0.04	0.00	94.27
29	0.15	0.16	0.22	0.01	93.26	0.04	0.00	0.00	0.00	0.00	93.84
Av.	0.11	0.21	0.34	0.01	92.99	0.06	0.01	0.02	0.02	0.00	93.78

**Table 2**

	L265	L270	L271	L273	L279	L280	L282	L283	L284	L285	L290	L291	Av.
SiO <sub>2</sub>	34.90	32.30	41.50	40.10	35.90	39.30	39.30	42.00	34.40	34.50	38.00	41.00	37.77
TiO <sub>2</sub>	0.88	0.70	0.22	0.39	0.19	0.37	0.48	0.37	0.30	0.19	0.11	0.16	0.36
Al <sub>2</sub> O <sub>3</sub>	7.52	0.97	3.86	3.49	1.62	2.96	3.99	6.00	0.95	0.76	0.77	1.72	2.88
Fe <sub>2</sub> O <sub>3</sub>	42.79	57.89	44.61	45.48	54.46	47.72	48.48	43.48	56.09	56.60	53.80	48.22	49.97
MnO	0.39	0.51	0.41	0.51	0.56	0.49	0.51	0.45	0.53	0.49	0.44	0.42	0.48
MgO	5.59	4.95	4.28	4.43	4.94	4.17	3.93	3.99	4.64	4.28	4.26	3.78	4.44
CaO	4.33	3.95	4.63	4.90	2.34	2.34	3.25	2.04	3.01	2.80	1.95	2.21	3.15
Na <sub>2</sub> O	2.05	0.32	1.16	1.22	0.42	0.88	1.19	1.74	0.26	0.19	0.22	0.56	0.85
K <sub>2</sub> O	1.96	0.17	0.97	0.98	0.43	0.86	1.03	1.76	0.18	0.15	0.13	0.53	0.76
P <sub>2</sub> O <sub>5</sub>	0.10	0.09	0.13	0.11	0.11	0.12	0.12	0.12	0.11	0.11	0.11	0.12	0.11
LOI	0.02	-1.83	-0.87	-1.08	-1.73	-1.55	-1.39	-1.13	-1.87	-1.83	-1.71	-1.07	-1.34
Total	100.53	100.02	100.90	100.52	99.23	97.67	100.89	100.81	98.60	98.24	98.07	97.65	99.43
Li	34.58	7.92	15.03	9.40	4.78	6.06	9.31	11.91	6.05	5.43	4.52	3.93	9.91
Sc	6.19	1.94	0.91	2.13	1.34	1.58	2.09	1.43	1.76	1.45	0.78	1.37	1.91
V	49.56	15.29	8.80	14.53	9.95	17.77	15.99	13.63	13.58	10.57	7.58	9.82	15.59
Cr	225.67	23.91	8.00	10.83	16.14	81.76	56.55	10.65	45.85	18.81	93.59	8.71	50.04
Ni	84.63	10.41	5.21	6.42	10.82	10.17	6.90	7.00	9.81	10.47	7.62	5.05	14.54
Cu	16.64	32.27	5.63	9.96	6.61	10.23	13.53	5.60	5.84	3.07	6.58	8.53	10.38
Zn	150.71	121.95	56.55	121.25	93.06	117.21	131.10	128.64	91.73	67.19	55.32	60.54	99.60
Rb	153.73	9.25	26.36	16.41	9.64	26.04	24.03	52.18	5.84	8.78	5.09	9.26	28.88
Sr	67.80	21.45	204.71	92.63	33.74	74.46	139.13	210.09	25.36	23.29	46.19	50.66	82.46
Y	28.99	16.84	16.08	24.41	16.04	17.58	23.55	17.54	21.14	16.72	11.00	10.99	18.41
Zr	111.46	19.08	14.04	20.64	27.31	32.03	44.59	30.12	34.23	15.15	12.80	7.44	30.74
Ba	75.26	16.82	152.90	147.08	43.24	89.29	133.28	200.46	20.50	24.61	34.91	93.38	85.98
Pb	3.28	0.66	1.51	1.73	0.76	1.70	1.91	2.47	0.61	0.47	0.67	0.90	1.39
Hf	4.53	0.87	0.67	1.07	1.07	1.28	1.73	1.23	1.21	0.77	0.44	0.26	1.26
Mo	3.49	5.62	2.05	2.74	3.18	3.07	4.42	2.65	3.10	2.22	1.84	0.78	2.93
Th	2.72	0.31	0.44	0.42	0.49	0.83	0.73	1.03	0.58	0.43	0.34	0.22	0.71
U	0.39	0.08	0.10	0.08	0.17	0.22	0.19	0.24	0.14	0.14	0.11	0.06	0.16
Cd	0.27	0.16	0.13	0.17	0.09	0.13	0.20	0.14	0.16	0.13	0.10	0.10	0.15
W	0.32	0.21	0.15	0.12	0.23	0.12	0.13	0.09	0.24	0.24	0.20	0.37	0.20
Re	1.90	1.45	2.23	1.89	1.10	0.23	1.55	1.52	1.83	1.16	1.49	1.90	1.52
Th/U	6.92	3.76	4.58	5.15	2.95	3.76	3.79	4.30	4.23	3.16	2.93	3.49	4.44
La	13.43	3.48	26.90	13.43	9.18	8.11	7.80	9.40	10.00	17.00	5.23	2.07	10.50
Ce	33.46	6.06	50.21	29.92	19.94	16.83	16.61	19.12	21.26	40.86	9.84	3.21	22.28
Pr	4.83	0.67	5.73	3.60	2.52	1.98	2.01	2.26	2.60	5.54	1.17	0.35	2.77
Nd	19.47	2.42	19.91	12.21	9.42	6.80	6.95	7.90	9.33	21.47	4.18	1.31	10.11
Sm	3.88	0.43	2.77	1.94	1.78	1.12	1.20	1.35	1.60	4.11	0.75	0.26	1.76
Eu	0.89	0.18	0.62	0.37	0.24	0.19	0.22	0.16	0.25	0.69	0.23	0.23	0.36
Gd	3.14	0.47	2.01	1.50	1.57	0.96	0.98	1.15	1.33	3.41	0.75	0.34	1.47
Tb	0.46	0.07	0.25	0.23	0.26	0.15	0.16	0.18	0.21	0.51	0.11	0.05	0.22
Dy	2.55	0.43	1.31	1.39	1.63	0.91	0.96	1.10	1.27	2.96	0.73	0.36	1.30
Ho	0.48	0.10	0.26	0.30	0.36	0.20	0.21	0.24	0.27	0.59	0.17	0.09	0.27
Er	1.30	0.30	0.71	0.93	1.11	0.61	0.67	0.78	0.85	1.69	0.51	0.27	0.81
Tm	0.19	0.05	0.10	0.15	0.19	0.10	0.11	0.13	0.14	0.26	0.08	0.04	0.13
Yb	1.21	0.30	0.65	1.10	1.38	0.70	0.79	0.95	1.02	1.80	0.55	0.26	0.89
Lu	0.19	0.05	0.10	0.17	0.23	0.11	0.12	0.15	0.16	0.29	0.09	0.04	0.14
LREE	75.96	13.24	106.15	61.47	43.08	35.04	34.78	40.18	45.04	89.66	21.40	7.43	47.78
HREE	9.52	1.76	5.39	5.77	6.72	3.75	4.00	4.68	5.25	11.51	2.99	1.47	5.23
Σ REE	85.48	15.00	111.54	67.25	49.79	38.79	38.78	44.86	50.29	101.17	24.38	8.90	53.02
LREE/HREE	7.98	7.52	19.69	10.65	6.41	9.36	8.69	8.58	8.58	7.79	7.17	5.06	8.96
(Eu/Eu*) <sub>SN</sub>	1.19	1.87	1.23	1.01	0.66	0.86	0.97	0.58	0.80	0.85	1.43	3.45	1.24
(Ce/Ce*) <sub>SN</sub>	0.93	0.91	0.93	0.99	0.95	0.96	0.96	0.95	0.96	0.95	0.91	0.85	0.94
(Y/Y*) <sub>SN</sub>	2.02	6.25	2.14	2.92	1.64	3.19	4.06	2.64	2.78	0.98	2.46	4.76	2.99
Y/Ho	59.89	166.73	61.86	80.84	45.20	87.92	111.09	72.17	77.44	28.14	66.64	123.52	81.79
(La/Yb) <sub>SN</sub>	0.82	0.87	3.03	0.90	0.49	0.85	0.72	0.73	0.73	0.70	0.70	0.58	0.93

(Eu/Eu\*)<sub>SN</sub> = [2Eu/(Sm+Gd)]<sub>SN</sub>; (Ce/Ce\*)<sub>SN</sub> = [2Ce/(La+Pr)]<sub>SN</sub>; (Y/Y\*)<sub>SN</sub> = [2Y/(Dy+Ho)]<sub>SN</sub>.



**Table 3**

	L266	L272	L274	L275	L276	L277	L278	L281	L286	L292	L293	Av.
SiO <sub>2</sub>	65.73	64.27	61.90	61.30	61.09	58.84	58.29	60.14	63.82	63.31	64.60	62.12
TiO <sub>2</sub>	0.02	0.06	0.31	0.42	0.48	0.74	0.66	0.62	0.15	0.06	0.10	0.33
Al <sub>2</sub> O <sub>3</sub>	18.39	18.91	17.35	17.10	17.75	17.88	17.29	15.29	17.79	16.98	18.81	17.59
Fe <sub>2</sub> O <sub>3</sub>	1.15	2.02	4.91	4.75	4.87	7.82	7.33	7.34	2.97	3.51	1.72	4.40
MnO	0.02	0.02	0.07	0.08	0.07	0.07	0.08	0.13	0.08	0.08	0.04	0.07
MgO	0.22	0.22	0.52	0.64	0.83	1.21	1.00	1.32	0.67	0.66	0.33	0.69
Na <sub>2</sub> O	5.88	7.07	5.63	5.55	6.03	6.21	4.98	5.20	5.91	5.60	6.57	5.88
CaO	0.76	1.18	1.72	1.94	1.80	1.11	1.68	3.30	1.07	1.72	1.19	1.59
K <sub>2</sub> O	6.89	5.05	6.28	6.20	5.62	5.21	7.05	4.83	5.78	5.87	5.92	5.88
P <sub>2</sub> O <sub>5</sub>	0.04	0.03	0.21	0.21	0.37	0.06	0.50	0.34	0.14	0.06	0.04	0.18
LOI	0.51	0.59	0.66	0.41	0.68	0.46	0.74	0.73	0.84	0.83	0.55	0.64
Total	99.62	99.43	99.56	98.62	99.58	99.60	99.63	99.23	99.23	98.69	99.85	99.37

Table 4

	SiO <sub>2</sub>	TiO <sub>2</sub>	Al <sub>2</sub> O <sub>3</sub>	Fe <sub>2</sub> O <sub>3</sub>	MnO	MgO	CaO	Na <sub>2</sub> O	K <sub>2</sub> O	P <sub>2</sub> O <sub>5</sub>	LOI	Li	Sc	V	Cr	Ni
TiO <sub>2</sub>	0.15															
Al <sub>2</sub> O <sub>3</sub>	0.13	0.34														
Fe <sub>2</sub> O <sub>3</sub>	0.52	0.07	0.77													
MnO	0.12	0.02	0.23	0.34												
MgO	0.50	0.40	0.05	0.02	0.00											
CaO	0.01	0.28	0.12	0.09	0.01	0.19										
Na <sub>2</sub> O	0.19	0.32	0.98	0.82	0.22	0.02	0.15									
K <sub>2</sub> O	0.18	0.29	0.99	0.80	0.22	0.02	0.08	0.98								
P <sub>2</sub> O <sub>5</sub>	0.65	0.30	0.01	0.21	0.08	0.55	0.02	0.02	0.02							
LOI	0.11	0.25	0.74	0.72	0.53	0.08	0.23	0.73	0.70	0.02						
Li	0.01	0.54	0.69	0.36	0.33	0.37	0.30	0.63	0.60	0.04	0.76					
Sc	0.11	0.69	0.44	0.14	0.11	0.50	0.20	0.39	0.38	0.21	0.52	0.78				
V	0.08	0.70	0.50	0.18	0.15	0.46	0.15	0.43	0.44	0.17	0.53	0.80	0.97			
Cr	0.09	0.37	0.25	0.08	0.19	0.34	0.02	0.19	0.20	0.13	0.30	0.55	0.68	0.76		
Ni	0.12	0.51	0.39	0.12	0.21	0.56	0.11	0.31	0.32	0.19	0.51	0.81	0.91	0.93	0.79	
Cu	0.22	0.58	0.00	0.03	0.00	0.20	0.15	0.00	0.00	0.36	0.00	0.06	0.15	0.14	0.05	0.07
Zn	0.02	0.71	0.42	0.13	0.03	0.17	0.09	0.42	0.42	0.19	0.13	0.28	0.44	0.46	0.19	0.25
Rb	0.00	0.52	0.73	0.38	0.31	0.32	0.10	0.65	0.67	0.05	0.72	0.92	0.82	0.88	0.65	0.87
Sr	0.58	0.00	0.41	0.55	0.12	0.15	0.03	0.46	0.43	0.40	0.19	0.08	0.01	0.00	0.03	0.02
Y	0.04	0.55	0.41	0.15	0.01	0.27	0.39	0.41	0.36	0.09	0.26	0.48	0.62	0.57	0.27	0.40
Zr	0.07	0.59	0.53	0.17	0.08	0.43	0.09	0.44	0.46	0.12	0.44	0.76	0.89	0.92	0.75	0.86
Ba	0.74	0.00	0.46	0.72	0.09	0.20	0.03	0.55	0.53	0.35	0.26	0.06	0.00	0.00	0.04	0.01
Pb	0.12	0.40	0.97	0.75	0.21	0.05	0.11	0.96	0.96	0.00	0.71	0.67	0.49	0.56	0.33	0.42
Hf	0.07	0.63	0.56	0.19	0.08	0.45	0.13	0.48	0.48	0.14	0.48	0.80	0.92	0.95	0.73	0.88
Mo	0.31	0.52	0.01	0.06	0.21	0.23	0.11	0.01	0.00	0.35	0.02	0.04	0.11	0.10	0.03	0.04
Th	0.02	0.52	0.65	0.28	0.19	0.35	0.06	0.56	0.59	0.07	0.56	0.83	0.84	0.91	0.74	0.88
U	0.01	0.37	0.58	0.21	0.07	0.22	0.00	0.47	0.55	0.04	0.32	0.57	0.59	0.70	0.62	0.65
Th/U	0.00	0.52	0.64	0.44	0.20	0.28	0.47	0.64	0.58	0.03	0.72	0.82	0.71	0.70	0.37	0.60
ΣREE	0.00	0.00	0.11	0.08	0.04	0.07	0.28	0.10	0.09	0.04	0.14	0.23	0.06	0.06	0.01	0.09
Eu/Eu*	0.01	0.01	0.06	0.00	0.20	0.05	0.00	0.05	0.05	0.01	0.02	0.02	0.00	0.01	0.01	0.00

	Cu	Zn	Rb	Sr	Y	Zr	Ba	Pb	Hf	Mo	Th	U	Th/U	ΣREE
Zn	0.27													
Rb	0.04	0.35												
Sr	0.06	0.02	0.05											
Y	0.06	0.61	0.42	0.01										
Zr	0.06	0.48	0.84	0.00	0.62									
Ba	0.05	0.07	0.05	0.84	0.04	0.00								
Pb	0.01	0.50	0.74	0.33	0.45	0.57	0.41							
Hf	0.07	0.50	0.87	0.00	0.66	0.99	0.00	0.60						
Mo	0.61	0.48	0.02	0.01	0.24	0.12	0.04	0.02	0.13					
Th	0.03	0.41	0.96	0.02	0.49	0.93	0.02	0.69	0.94	0.04				
U	0.00	0.44	0.77	0.03	0.38	0.82	0.02	0.62	0.80	0.06	0.88			
Th/U	0.05	0.35	0.71	0.07	0.64	0.61	0.11	0.65	0.66	0.03	0.64	0.36		
ΣREE	0.14	0.01	0.12	0.09	0.16	0.07	0.03	0.07	0.09	0.02	0.10	0.06	0.19	
Eu/Eu*	0.07	0.13	0.02	0.06	0.20	0.07	0.01	0.06	0.07	0.10	0.06	0.18	0.01	0.23

## Appendix A.

### A.1.

No.	SiO <sub>2</sub>	TiO <sub>2</sub>	Al <sub>2</sub> O <sub>3</sub>	Cr <sub>2</sub> O <sub>3</sub>	FeO <sub>t</sub>	MnO	MgO	CaO	Na <sub>2</sub> O	K <sub>2</sub> O	Total
1	0.05	0.09	0.06	0.00	92.56	0.02	0.00	0.01	0.02	0.02	92.84
2	0.09	0.07	0.00	0.00	91.04	0.00	0.03	0.03	0.05	0.02	91.33
3	0.09	0.07	0.03	0.03	92.15	0.00	0.00	0.05	0.10	0.01	92.52
4	0.09	0.07	0.07	0.02	92.51	0.01	0.01	0.00	0.01	0.00	92.80
5	0.13	0.17	0.04	0.02	92.89	0.01	0.01	0.02	0.05	0.01	93.34
6	0.08	0.10	0.07	0.00	92.61	0.01	0.00	0.00	0.00	0.01	92.88
7	0.12	0.07	0.04	0.00	92.66	0.02	0.00	0.00	0.03	0.00	92.95
8	0.08	0.07	0.08	0.00	92.92	0.01	0.02	0.01	0.07	0.01	93.25
9	0.07	0.10	0.09	0.00	93.06	0.03	0.00	0.00	0.00	0.00	93.36
10	0.08	0.12	0.08	0.02	92.77	0.00	0.00	0.01	0.00	0.00	93.08
11	0.07	0.09	0.07	0.00	92.84	0.01	0.00	0.00	0.03	0.00	93.11
12	0.09	0.08	0.10	0.02	92.68	0.01	0.00	0.01	0.04	0.00	93.03
13	0.13	0.07	0.12	0.01	92.90	0.02	0.00	0.00	0.01	0.00	93.27
14	0.07	0.09	0.05	0.01	93.04	0.01	0.00	0.02	0.00	0.01	93.30
15	0.06	0.08	0.08	0.02	93.05	0.00	0.00	0.03	0.06	0.00	93.39
16	0.05	0.11	0.05	0.00	93.03	0.03	0.00	0.00	0.00	0.01	93.28
17	0.10	0.05	0.15	0.04	92.45	0.03	0.00	0.09	0.01	0.00	92.94
18	0.07	0.07	0.05	0.01	92.73	0.02	0.00	0.03	0.02	0.01	93.01
19	0.03	0.10	0.07	0.00	92.88	0.00	0.00	0.05	0.06	0.01	93.21
Av.	0.08	0.09	0.07	0.01	92.67	0.01	0.00	0.02	0.03	0.01	92.99

## A.2.

No.	1	2	3	4	5	6	7	8	9	10	11	12	Av.
SiO <sub>2</sub>	51.26	51.70	51.55	51.73	51.31	52.02	52.15	52.43	52.43	52.25	52.37	52.14	51.95
TiO <sub>2</sub>	0.09	0.09	0.10	0.11	0.08	0.06	0.07	0.09	0.06	0.14	0.13	0.14	0.10
Al <sub>2</sub> O <sub>3</sub>	0.72	0.91	0.80	0.91	0.79	0.77	0.71	0.71	0.59	1.08	1.01	0.92	0.83
Cr <sub>2</sub> O <sub>3</sub>	0.00	0.00	0.01	0.00	0.01	0.00	0.00	0.01	0.00	0.00	0.00	0.01	0.00
FeO <sub>t</sub>	15.24	14.81	15.03	15.24	14.87	14.87	15.20	15.08	14.86	15.00	14.84	15.09	15.01
MnO	0.70	0.68	0.65	0.68	0.67	0.65	0.68	0.67	0.64	0.67	0.66	0.70	0.67
MgO	9.81	9.68	9.96	9.53	9.63	9.89	9.83	9.78	9.79	9.62	9.77	9.78	9.76
CaO	20.01	19.97	20.31	20.09	20.48	20.38	20.29	20.35	20.60	20.19	20.45	20.36	20.29
Na <sub>2</sub> O	1.02	1.05	1.10	1.13	1.16	1.06	1.06	1.02	0.96	1.07	1.05	1.05	1.06
K <sub>2</sub> O	0.00	0.00	0.01	0.00	0.00	0.00	0.00	0.00	0.00	0.00	0.00	0.01	0.00
Total	98.86	98.90	99.52	99.42	99.00	99.70	99.98	100.13	99.93	100.02	100.29	100.20	99.66
Cations per 6 oxygens													
Si	1.980	1.995	1.974	1.987	1.976	1.990	1.991	2.000	2.004	1.995	1.992	1.987	1.989
Ti	0.003	0.003	0.003	0.003	0.002	0.002	0.002	0.003	0.002	0.004	0.004	0.004	0.003
Al	0.033	0.042	0.036	0.041	0.036	0.035	0.032	0.032	0.027	0.049	0.046	0.041	0.037
Cr	0.000	0.000	0.000	0.000	0.000	0.000	0.000	0.000	0.000	0.000	0.000	0.000	0.000
Fe <sup>3+</sup>	0.079	0.042	0.092	0.063	0.094	0.061	0.060	0.039	0.034	0.034	0.040	0.055	0.058
Fe <sup>2+</sup>	0.413	0.436	0.390	0.427	0.386	0.415	0.425	0.443	0.441	0.445	0.432	0.426	0.423
Mn	0.023	0.022	0.021	0.022	0.022	0.021	0.022	0.022	0.021	0.022	0.021	0.023	0.022
Mg	0.565	0.557	0.569	0.546	0.553	0.564	0.559	0.556	0.558	0.547	0.554	0.555	0.557
Ca	0.828	0.826	0.833	0.827	0.845	0.835	0.830	0.832	0.844	0.826	0.834	0.831	0.832
Na	0.077	0.079	0.082	0.084	0.086	0.078	0.078	0.075	0.071	0.079	0.078	0.078	0.079
K	0.000	0.000	0.001	0.000	0.000	0.000	0.000	0.000	0.000	0.000	0.000	0.000	0.000
Wo	0.405	0.411	0.405	0.408	0.412	0.413	0.412	0.416	0.422	0.412	0.415	0.411	0.412
En	0.282	0.278	0.284	0.273	0.276	0.282	0.280	0.278	0.279	0.274	0.277	0.278	0.278
Fs	0.207	0.218	0.195	0.213	0.193	0.207	0.212	0.221	0.220	0.223	0.216	0.213	0.212
Ae	0.077	0.042	0.082	0.063	0.087	0.061	0.060	0.039	0.034	0.034	0.040	0.055	0.056
Jd	0.000	0.036	0.000	0.022	0.000	0.017	0.018	0.032	0.027	0.043	0.038	0.023	0.021
Mg#	0.577	0.561	0.593	0.561	0.589	0.576	0.568	0.557	0.558	0.551	0.562	0.566	0.568
XFe	0.423	0.439	0.407	0.439	0.411	0.424	0.432	0.443	0.442	0.449	0.438	0.434	0.432

### A.3.

No.	1	2	3	4	5	6	7	8	9	10	11	12	13	14	15	16	Av.
SiO <sub>2</sub>	64.20	63.61	63.71	63.23	64.29	64.15	64.66	64.60	64.43	64.64	64.00	64.58	64.45	64.51	64.51	64.51	64.26
TiO <sub>2</sub>	0.03	0.02	0.06	0.06	0.05	0.04	0.03	0.03	0.04	0.06	0.03	0.05	0.05	0.03	0.03	0.03	0.04
Al <sub>2</sub> O <sub>3</sub>	18.53	18.25	18.26	18.23	18.53	18.39	18.09	18.51	18.25	18.25	18.28	18.45	18.21	18.24	18.23	18.19	18.31
Cr <sub>2</sub> O <sub>3</sub>	0.01	0.00	0.01	0.00	0.00	0.00	0.00	0.00	0.00	0.00	0.01	0.03	0.02	0.02	0.01	0.00	0.01
FeO <sub>t</sub>	0.00	0.07	0.06	0.17	0.07	0.19	0.06	0.01	0.01	0.05	0.02	0.25	0.21	0.03	0.06	0.02	0.00
MnO	0.01	0.00	0.01	0.01	0.01	0.00	0.02	0.00	0.01	0.02	0.01	0.00	0.00	0.00	0.00	0.00	0.01
MgO	0.00	0.00	0.00	0.00	0.01	0.03	0.00	0.00	0.00	0.00	0.00	0.00	0.01	0.00	0.01	0.02	0.01
CaO	0.00	0.01	0.00	0.00	0.00	0.00	0.01	0.01	0.00	0.02	0.00	0.00	0.00	0.01	0.00	0.00	0.00
Na <sub>2</sub> O	0.32	0.37	0.32	0.21	0.35	0.24	0.23	0.28	0.32	0.30	0.29	0.26	0.26	0.28	0.32	0.31	0.29
K <sub>2</sub> O	16.81	16.52	16.77	16.78	16.66	16.87	16.89	16.94	16.80	16.86	16.84	17.03	16.80	16.93	16.72	16.89	16.82
Total	99.90	98.85	99.19	98.69	99.98	99.91	99.99	100.38	99.86	100.21	99.48	100.65	100.00	100.04	99.88	99.97	99.82
Cations per 8 oxygens																	
Si	2.969	2.973	2.968	2.962	2.971	2.969	2.991	2.974	2.982	2.982	2.973	2.967	2.982	2.981	2.986	2.982	2.976
Ti	0.001	0.001	0.002	0.002	0.002	0.002	0.001	0.001	0.001	0.002	0.001	0.002	0.002	0.001	0.001	0.001	0.001
Al	1.010	1.005	1.003	1.007	1.009	1.003	0.986	1.004	0.995	0.992	1.001	0.999	0.993	0.993	0.994	0.991	0.999
Cr	0.000	0.000	0.000	0.000	0.000	0.000	0.000	0.000	0.000	0.000	0.001	0.001	0.001	0.001	0.000	0.000	0.000
Fe <sup>3+</sup>	0.000	0.003	0.002	0.007	0.003	0.007	0.002	0.000	0.000	0.002	0.001	0.010	0.008	0.001	0.002	0.001	0.003
Fe <sup>2+</sup>	0.000	0.000	0.000	0.000	0.000	0.000	0.000	0.000	0.000	0.000	0.000	0.000	0.000	0.000	0.000	0.000	0.000
Mn	0.000	0.000	0.000	0.000	0.000	0.000	0.001	0.000	0.000	0.001	0.000	0.000	0.000	0.000	0.000	0.000	0.000
Mg	0.000	0.000	0.000	0.000	0.001	0.002	0.000	0.000	0.000	0.000	0.000	0.000	0.001	0.000	0.001	0.001	0.000
Ca	0.000	0.001	0.000	0.000	0.000	0.000	0.000	0.000	0.000	0.001	0.000	0.000	0.000	0.000	0.000	0.000	0.000
Na	0.028	0.033	0.029	0.020	0.031	0.021	0.021	0.025	0.029	0.027	0.026	0.023	0.023	0.025	0.028	0.028	0.026
K	0.992	0.985	0.997	1.003	0.982	0.996	0.997	0.995	0.992	0.992	0.998	0.998	0.991	0.998	0.987	0.996	0.994
Xan	0.000	0.001	0.000	0.000	0.000	0.000	0.000	0.000	0.000	0.001	0.000	0.000	0.000	0.000	0.000	0.000	0.000
Xab	0.028	0.032	0.028	0.019	0.031	0.021	0.021	0.025	0.028	0.026	0.025	0.023	0.023	0.024	0.028	0.027	0.026
Xor	0.972	0.967	0.972	0.981	0.969	0.979	0.979	0.975	0.972	0.972	0.975	0.977	0.977	0.975	0.972	0.973	0.974

**A.4.**

No.	1	2	3	4	5	6	7	8	9	10	11	12	13	Av.
SiO <sub>2</sub>	67.65	66.64	67.65	67.08	74.33	66.82	66.26	66.58	67.22	67.14	67.37	67.21	67.29	67.63
TiO <sub>2</sub>	0.03	0.03	0.04	0.03	0.04	0.04	0.06	0.04	0.01	0.04	0.00	0.02	0.03	0.03
Al <sub>2</sub> O <sub>3</sub>	20.74	20.13	20.28	20.59	13.69	21.37	21.62	21.35	21.11	20.61	21.09	20.77	21.22	20.35
Cr <sub>2</sub> O <sub>3</sub>	0.01	0.00	0.00	0.01	0.02	0.01	0.00	0.02	0.01	0.01	0.03	0.00	0.02	0.01
FeO <sub>t</sub>	0.02	0.08	0.02	0.12	0.06	0.05	0.13	0.04	0.10	0.26	0.07	0.05	0.05	0.08
MnO	0.00	0.00	0.01	0.01	0.00	0.00	0.01	0.03	0.02	0.00	0.00	0.01	0.00	0.01
MgO	0.00	0.00	0.00	0.00	0.00	0.01	0.00	0.00	0.00	0.01	0.02	0.01	0.00	0.00
CaO	1.56	1.29	1.05	1.31	1.08	1.71	1.50	1.62	1.35	1.31	1.29	1.35	1.21	1.36
Na <sub>2</sub> O	9.12	10.28	10.16	10.34	7.86	10.09	10.16	10.21	10.38	10.37	10.43	10.39	10.47	10.02
K <sub>2</sub> O	0.07	0.06	0.07	0.07	0.07	0.07	0.07	0.11	0.08	0.08	0.08	0.09	0.08	0.08
Total	99.20	98.51	99.27	99.56	97.15	100.18	99.80	99.99	100.28	99.83	100.39	99.90	100.37	99.57
Cations per 8 oxygens														
Si	3.031	2.979	3.006	2.967	3.472	2.941	2.924	2.933	2.951	2.963	2.954	2.961	2.949	3.002
Ti	0.001	0.001	0.001	0.001	0.001	0.001	0.002	0.001	0.000	0.001	0.000	0.001	0.001	0.001
Al	1.095	1.061	1.062	1.073	0.754	1.109	1.125	1.108	1.092	1.072	1.090	1.079	1.096	1.063
Cr	0.000	0.000	0.000	0.000	0.001	0.001	0.000	0.001	0.000	0.000	0.001	0.000	0.001	0.000
Fe <sup>3+</sup>	0.000	0.000	0.000	0.000	0.000	0.000	0.000	0.000	0.000	0.000	0.000	0.000	0.000	0.000
Fe <sup>2+</sup>	0.001	0.003	0.001	0.005	0.002	0.002	0.005	0.001	0.004	0.010	0.003	0.002	0.002	0.003
Mn	0.000	0.000	0.000	0.000	0.000	0.000	0.000	0.001	0.001	0.000	0.000	0.000	0.000	0.000
Mg	0.000	0.000	0.000	0.000	0.000	0.001	0.000	0.000	0.000	0.001	0.001	0.001	0.000	0.000
Ca	0.075	0.062	0.050	0.062	0.054	0.081	0.071	0.077	0.064	0.062	0.061	0.064	0.057	0.064
Na	0.792	0.891	0.875	0.887	0.712	0.861	0.869	0.872	0.884	0.887	0.887	0.888	0.890	0.861
K	0.004	0.004	0.004	0.004	0.004	0.004	0.004	0.006	0.005	0.005	0.005	0.005	0.005	0.004
Xan	0.086	0.065	0.054	0.065	0.070	0.085	0.075	0.080	0.067	0.065	0.064	0.067	0.060	0.069
Xab	0.909	0.932	0.942	0.931	0.924	0.911	0.921	0.914	0.928	0.930	0.931	0.928	0.936	0.926
Xor	0.005	0.004	0.004	0.004	0.005	0.004	0.004	0.006	0.005	0.005	0.005	0.005	0.005	0.005

**A.5.**

No.	1	2	3	4	5	6	7	8	Av.
SiO <sub>2</sub>	0.02	0.02	0.03	0.03	0.03	0.02	0.02	0.01	0.02
TiO <sub>2</sub>	50.17	50.59	50.29	51.32	51.18	50.83	50.77	50.36	50.69
Al <sub>2</sub> O <sub>3</sub>	0.01	0.02	0.00	0.00	0.01	0.00	0.03	0.00	0.01
Cr <sub>2</sub> O <sub>3</sub>	0.02	0.01	0.00	0.02	0.01	0.01	0.00	0.00	0.01
FeO <sub>t</sub>	43.55	44.38	44.79	42.74	42.58	44.01	44.11	44.45	43.83
MnO	4.14	4.22	4.01	5.03	4.96	4.25	4.21	4.19	4.38
MgO	0.07	0.03	0.04	0.01	0.01	0.03	0.06	0.01	0.03
CaO	0.08	0.00	0.01	0.09	0.14	0.01	0.00	0.01	0.04
Na <sub>2</sub> O	0.05	0.02	0.02	0.04	0.00	0.00	0.00	0.02	0.02
K <sub>2</sub> O	0.00	0.00	0.00	0.00	0.00	0.00	0.01	0.00	0.00
Total	98.09	99.28	99.19	99.29	98.92	99.17	99.21	99.07	99.03

## Appendix B.

### B.1.

No.	1	2	3	4	5	6	7	8	9	10	11	12	13	14	15
SiO <sub>2</sub>	51.69	51.35	51.12	48.95	51.39	51.35	50.55	52.00	52.05	52.12	52.00	52.01	51.92	52.08	51.90
TiO <sub>2</sub>	0.01	0.03	0.04	0.04	0.04	0.06	0.04	0.06	0.05	0.04	0.01	0.06	0.06	0.05	0.06
Al <sub>2</sub> O <sub>3</sub>	0.26	0.24	0.23	0.28	0.25	0.20	0.22	0.32	0.28	0.26	0.27	0.29	0.28	0.25	0.30
Cr <sub>2</sub> O <sub>3</sub>	0.00	0.00	0.00	0.00	0.01	0.00	0.03	0.00	0.00	0.00	0.02	0.00	0.00	0.00	0.00
FeO <sub>i</sub>	17.55	17.60	17.36	21.75	17.54	20.06	18.96	16.48	19.33	17.53	17.48	18.76	17.14	18.15	17.35
MnO	0.49	0.55	0.50	0.50	0.54	0.58	0.55	0.50	0.60	0.54	0.54	0.57	0.52	0.54	0.49
MgO	9.33	9.24	9.27	9.18	9.33	9.51	9.20	9.41	9.38	9.36	9.13	9.76	9.43	9.70	9.24
CaO	20.85	20.30	20.59	19.22	20.43	18.28	19.47	20.71	18.94	19.83	20.55	18.19	20.67	18.84	20.44
Na <sub>2</sub> O	0.73	0.69	0.73	0.70	0.71	0.58	0.70	0.69	0.69	0.72	0.70	0.77	0.74	0.73	0.74
K <sub>2</sub> O	0.00	0.00	0.00	0.00	0.02	0.00	0.01	0.00	0.00	0.02	0.02	0.02	0.01	0.00	0.00
Total	100.92	100.00	99.83	100.62	100.26	100.62	99.73	100.18	101.33	100.42	100.73	100.43	100.76	100.35	100.52
Cations per 6 oxygens															
Si	1.974	1.981	1.973	1.891	1.976	1.979	1.961	1.996	1.988	2.001	1.992	1.998	1.984	2.001	1.990
Ti	0.000	0.001	0.001	0.001	0.001	0.002	0.001	0.002	0.001	0.001	0.000	0.002	0.002	0.002	0.002
Al	0.012	0.011	0.011	0.013	0.011	0.009	0.010	0.015	0.013	0.012	0.012	0.013	0.013	0.011	0.014
Cr	0.000	0.000	0.000	0.000	0.000	0.000	0.001	0.000	0.000	0.000	0.001	0.000	0.000	0.000	0.000
Fe <sup>3+</sup>	0.095	0.078	0.096	0.257	0.088	0.073	0.119	0.041	0.059	0.039	0.057	0.046	0.072	0.038	0.059
Fe <sup>2+</sup>	0.466	0.490	0.464	0.446	0.476	0.574	0.496	0.488	0.559	0.524	0.503	0.557	0.476	0.545	0.497
Mn	0.016	0.018	0.017	0.016	0.018	0.019	0.018	0.016	0.020	0.018	0.018	0.019	0.017	0.018	0.016
Mg	0.531	0.531	0.533	0.528	0.535	0.546	0.532	0.538	0.534	0.536	0.521	0.559	0.537	0.555	0.528
Ca	0.853	0.839	0.851	0.795	0.842	0.755	0.809	0.852	0.775	0.816	0.843	0.749	0.846	0.776	0.840
Na	0.054	0.052	0.054	0.053	0.053	0.044	0.053	0.052	0.051	0.054	0.052	0.057	0.055	0.055	0.055
K	0.000	0.000	0.000	0.000	0.001	0.000	0.001	0.000	0.000	0.001	0.001	0.001	0.000	0.000	0.000
Wo	0.421	0.414	0.421	0.392	0.416	0.374	0.400	0.425	0.382	0.408	0.418	0.374	0.418	0.388	0.415
En	0.265	0.266	0.267	0.264	0.267	0.273	0.266	0.269	0.267	0.268	0.261	0.279	0.268	0.278	0.264
Fs	0.233	0.245	0.232	0.223	0.238	0.287	0.248	0.244	0.279	0.262	0.252	0.278	0.238	0.272	0.249
Ae	0.054	0.052	0.054	0.053	0.054	0.044	0.053	0.041	0.051	0.039	0.053	0.046	0.055	0.038	0.055
Jd	0.000	0.000	0.000	0.000	0.000	0.000	0.000	0.011	0.000	0.012	0.000	0.011	0.000	0.011	0.000
Mg#	0.533	0.520	0.534	0.542	0.529	0.488	0.517	0.525	0.489	0.505	0.509	0.501	0.530	0.505	0.515
XFe	0.467	0.480	0.466	0.458	0.471	0.512	0.483	0.475	0.511	0.495	0.491	0.499	0.470	0.495	0.485



## B.1. (Continued)

No.	16	17	18	19	20	21	22	23	24	25	26	27	28	29	30	Av.
SiO <sub>2</sub>	51.83	51.96	51.90	51.58	51.94	52.12	51.77	52.01	51.97	51.96	51.88	51.65	51.66	51.89	51.38	51.67
TiO <sub>2</sub>	0.06	0.07	0.05	0.09	0.05	0.07	0.07	0.06	0.07	0.09	0.07	0.07	0.06	0.07	0.07	0.06
Al <sub>2</sub> O <sub>3</sub>	0.27	0.30	0.32	0.27	0.25	0.24	0.25	0.27	0.26	0.59	0.56	0.53	0.56	0.56	0.56	0.32
Cr <sub>2</sub> O <sub>3</sub>	0.01	0.00	0.00	0.01	0.00	0.01	0.00	0.00	0.00	0.03	0.00	0.02	0.01	0.00	0.00	0.01
FeO <sub>t</sub>	17.39	16.83	17.34	17.14	16.80	16.89	16.99	17.14	17.33	16.60	16.91	16.49	16.82	16.87	16.76	17.58
MnO	0.50	0.50	0.51	0.49	0.50	0.51	0.52	0.50	0.52	0.60	0.55	0.56	0.61	0.64	0.56	0.54
MgO	9.39	9.33	9.24	9.18	9.24	9.11	9.04	9.42	9.25	9.36	9.42	9.35	9.32	9.24	9.21	9.32
CaO	20.76	20.73	20.55	20.47	20.75	20.70	20.60	20.49	20.83	20.15	20.50	20.42	20.00	20.42	20.60	20.18
Na <sub>2</sub> O	0.71	0.77	0.77	0.75	0.72	0.71	0.69	0.72	0.79	0.94	0.87	0.91	0.95	0.80	0.86	0.75
K <sub>2</sub> O	0.00	0.00	0.00	0.00	0.01	0.01	0.04	0.00	0.00	0.00	0.02	0.00	0.00	0.00	0.00	0.01
Total	100.93	100.50	100.67	99.99	100.27	100.38	99.97	100.61	101.02	100.31	100.78	100.00	100.00	100.51	99.99	100.42
Cations per 6 oxygens																
Si	1.979	1.989	1.986	1.988	1.995	2.001	1.997	1.990	1.982	1.989	1.978	1.983	1.985	1.987	1.975	1.983
Ti	0.002	0.002	0.001	0.003	0.002	0.002	0.002	0.002	0.002	0.003	0.002	0.002	0.002	0.002	0.002	0.002
Al	0.012	0.013	0.014	0.012	0.011	0.011	0.012	0.012	0.012	0.027	0.025	0.024	0.026	0.025	0.025	0.015
Cr	0.000	0.000	0.000	0.000	0.000	0.000	0.000	0.000	0.000	0.001	0.000	0.001	0.000	0.000	0.000	0.000
Fe <sup>3+</sup>	0.079	0.062	0.068	0.063	0.051	0.036	0.044	0.058	0.079	0.059	0.080	0.073	0.072	0.057	0.085	0.073
Fe <sup>2+</sup>	0.476	0.477	0.487	0.489	0.489	0.507	0.504	0.491	0.473	0.473	0.459	0.456	0.468	0.483	0.454	0.492
Mn	0.016	0.016	0.016	0.016	0.016	0.017	0.017	0.016	0.017	0.020	0.018	0.018	0.020	0.021	0.018	0.017
Mg	0.534	0.532	0.527	0.527	0.529	0.521	0.520	0.537	0.526	0.534	0.535	0.535	0.534	0.527	0.528	0.533
Ca	0.849	0.850	0.843	0.845	0.854	0.852	0.851	0.840	0.851	0.827	0.837	0.840	0.823	0.838	0.849	0.830
Na	0.052	0.057	0.057	0.056	0.054	0.053	0.052	0.054	0.058	0.069	0.064	0.068	0.071	0.060	0.064	0.056
K	0.000	0.000	0.000	0.000	0.000	0.000	0.002	0.000	0.000	0.000	0.001	0.000	0.000	0.000	0.000	0.000
Wo	0.419	0.421	0.415	0.418	0.425	0.426	0.425	0.416	0.421	0.409	0.409	0.412	0.405	0.413	0.413	0.410
En	0.267	0.266	0.264	0.264	0.264	0.261	0.260	0.269	0.263	0.267	0.268	0.267	0.267	0.264	0.264	0.267
Fs	0.238	0.238	0.243	0.245	0.244	0.253	0.252	0.245	0.237	0.236	0.230	0.228	0.234	0.242	0.227	0.246
Ae	0.052	0.058	0.057	0.056	0.051	0.036	0.044	0.054	0.058	0.059	0.065	0.068	0.071	0.057	0.064	0.053
Jd	0.000	0.000	0.000	0.000	0.003	0.011	0.008	0.000	0.000	0.011	0.000	0.000	0.000	0.003	0.000	0.003
Mg#	0.529	0.528	0.520	0.519	0.520	0.507	0.508	0.523	0.526	0.530	0.538	0.540	0.533	0.522	0.537	0.521
XFe	0.471	0.473	0.480	0.481	0.480	0.493	0.492	0.477	0.474	0.470	0.462	0.460	0.467	0.478	0.463	0.480

## B.2.

No.	1	2	3	4	5	6	7	8	9	10	11	12	13	14	15	16	17	18	Av.
SiO <sub>2</sub>	49.13	49.80	49.44	49.90	49.23	50.08	50.17	50.11	50.36	50.06	50.19	50.12	50.10	50.06	50.05	49.97	50.17	50.34	49.96
TiO <sub>2</sub>	0.06	0.06	0.04	0.03	0.05	0.08	0.06	0.05	0.07	0.03	0.05	0.04	0.05	0.03	0.07	0.06	0.07	0.10	0.06
Al <sub>2</sub> O <sub>3</sub>	0.04	0.03	0.03	0.02	0.02	0.07	0.10	0.07	0.09	0.05	0.03	0.08	0.07	0.15	0.14	0.18	0.15	0.14	0.08
Cr <sub>2</sub> O <sub>3</sub>	0.00	0.00	0.00	0.01	0.00	0.00	0.00	0.00	0.00	0.00	0.01	0.00	0.01	0.00	0.01	0.00	0.01	0.00	0.00
FeO <sub>t</sub>	38.14	37.92	37.95	37.99	37.49	37.18	37.25	37.62	37.24	37.37	37.38	37.42	37.12	36.71	36.67	36.71	36.95	36.96	37.34
MnO	1.27	1.28	1.26	1.26	1.25	1.28	1.35	1.30	1.24	1.25	1.24	1.26	1.23	1.55	1.54	1.53	1.47	1.52	1.34
MgO	11.68	11.94	11.67	11.65	12.05	11.84	11.65	11.69	11.89	11.51	11.60	11.54	11.54	11.81	11.88	11.73	11.80	11.75	11.73
CaO	0.61	0.62	0.63	0.61	0.61	0.63	0.67	0.65	0.61	0.66	0.68	0.58	0.64	0.75	0.60	0.61	0.65	0.58	0.63
Na <sub>2</sub> O	0.01	0.03	0.02	0.04	0.01	0.01	0.02	0.03	0.02	0.02	0.01	0.05	0.03	0.05	0.00	0.00	0.02	0.00	0.02
K <sub>2</sub> O	0.00	0.00	0.01	0.01	0.00	0.00	0.00	0.00	0.00	0.01	0.02	0.01	0.00	0.00	0.01	0.00	0.01	0.00	0.00
Total	100.93	101.68	101.05	101.53	100.72	101.17	101.27	101.52	101.52	100.96	101.21	101.09	100.80	101.11	100.97	100.78	101.29	101.39	101.17
Cations per 6 oxygens																			
Si	1.960	1.969	1.969	1.978	1.963	1.988	1.992	1.985	1.992	1.995	1.995	1.994	1.999	1.987	1.990	1.992	1.989	1.995	1.985
Ti	0.002	0.002	0.001	0.001	0.002	0.002	0.002	0.001	0.002	0.001	0.001	0.001	0.001	0.001	0.002	0.002	0.002	0.003	0.002
Al	0.002	0.001	0.001	0.001	0.001	0.003	0.005	0.003	0.004	0.002	0.002	0.004	0.004	0.007	0.007	0.008	0.007	0.006	0.004
Cr	0.000	0.000	0.000	0.001	0.000	0.000	0.000	0.000	0.000	0.000	0.001	0.000	0.000	0.000	0.000	0.000	0.000	0.000	0.000
Fe <sup>3+</sup>	0.076	0.061	0.060	0.044	0.071	0.017	0.010	0.026	0.010	0.008	0.008	0.010	0.000	0.021	0.010	0.005	0.012	0.000	0.025
Fe <sup>2+</sup>	1.196	1.193	1.204	1.215	1.179	1.218	1.227	1.220	1.222	1.238	1.234	1.236	1.239	1.198	1.210	1.219	1.214	1.225	1.216
Mn	0.043	0.043	0.043	0.042	0.042	0.043	0.045	0.044	0.042	0.042	0.042	0.042	0.042	0.052	0.052	0.052	0.049	0.051	0.045
Mg	0.694	0.703	0.693	0.688	0.716	0.701	0.689	0.690	0.701	0.684	0.687	0.684	0.686	0.699	0.704	0.697	0.697	0.694	0.695
Ca	0.026	0.026	0.027	0.026	0.026	0.027	0.029	0.028	0.026	0.028	0.029	0.025	0.028	0.032	0.026	0.026	0.028	0.025	0.027
Na	0.001	0.003	0.002	0.003	0.000	0.001	0.002	0.003	0.001	0.002	0.001	0.004	0.002	0.004	0.000	0.000	0.001	0.000	0.002
K	0.000	0.000	0.000	0.000	0.000	0.000	0.000	0.000	0.000	0.001	0.001	0.001	0.000	0.000	0.001	0.000	0.000	0.000	0.000
Wo	0.013	0.013	0.013	0.013	0.013	0.013	0.014	0.014	0.013	0.014	0.014	0.012	0.014	0.016	0.013	0.013	0.014	0.012	0.013
En	0.347	0.352	0.346	0.344	0.358	0.350	0.344	0.345	0.350	0.342	0.343	0.342	0.343	0.348	0.351	0.347	0.348	0.347	0.347
Fs	0.598	0.596	0.602	0.607	0.589	0.608	0.613	0.609	0.610	0.618	0.617	0.617	0.619	0.597	0.603	0.608	0.605	0.612	0.607
Mg <sup>#</sup>	0.367	0.371	0.365	0.362	0.378	0.365	0.360	0.361	0.364	0.356	0.358	0.356	0.357	0.368	0.368	0.364	0.365	0.362	0.364
XFe	0.633	0.629	0.635	0.638	0.622	0.635	0.640	0.639	0.636	0.644	0.642	0.644	0.644	0.632	0.632	0.636	0.635	0.638	0.636

**B.3.**

No.	1	2	3	4	5	6	7	8	9	Av.
SiO <sub>2</sub>	41.81	41.67	41.93	41.81	41.86	42.17	40.92	41.94	41.89	41.78
TiO <sub>2</sub>	1.18	1.13	1.14	1.10	1.11	1.11	1.02	1.07	0.97	1.09
Al <sub>2</sub> O <sub>3</sub>	10.65	10.68	10.89	10.66	10.75	10.42	10.85	10.42	10.82	10.68
Cr <sub>2</sub> O <sub>3</sub>	0.00	0.00	0.00	0.00	0.00	0.00	0.00	0.00	0.00	0.00
FeO <sub>t</sub>	19.59	19.49	19.45	19.45	19.23	19.32	20.69	19.10	19.41	19.53
MnO	0.69	0.74	0.71	0.64	0.67	0.61	0.64	0.62	0.67	0.67
MgO	9.19	9.20	9.18	9.59	9.53	9.61	9.51	9.56	9.48	9.43
CaO	10.76	10.56	10.70	10.81	10.69	10.72	9.62	10.84	10.66	10.60
Na <sub>2</sub> O	2.14	2.19	2.13	2.23	2.24	2.25	2.01	2.20	2.23	2.18
K <sub>2</sub> O	1.72	1.69	1.57	1.68	1.62	1.68	1.55	1.74	1.64	1.65
Total	97.73	97.35	97.71	97.97	97.70	97.89	96.81	97.50	97.77	97.60
Cations per 23 oxygens										
Si	6.436	6.440	6.442	6.407	6.429	6.470	6.341	6.459	6.430	6.428
Al <sup>IV</sup>	1.564	1.560	1.558	1.593	1.571	1.530	1.659	1.541	1.570	1.572
Sum T	8.000	8.000	8.000	8.000	8.000	8.000	8.000	8.000	8.000	8.000
Al <sup>VI</sup>	0.369	0.385	0.413	0.332	0.375	0.354	0.323	0.351	0.387	0.365
Cr	0.000	0.000	0.000	0.000	0.000	0.000	0.000	0.001	0.000	0.000
Ti	0.137	0.131	0.132	0.127	0.128	0.129	0.118	0.124	0.112	0.126
Fe <sup>3+</sup>	0.000	0.000	0.000	0.016	0.000	0.000	0.189	0.000	0.000	0.023
Mg	2.109	2.119	2.102	2.190	2.181	2.197	2.196	2.194	2.169	2.162
Fe <sup>2+</sup>	2.522	2.519	2.499	2.477	2.470	2.479	2.492	2.460	2.492	2.490
Sum C	5.136	5.154	5.146	5.142	5.155	5.159	5.319	5.130	5.159	5.167
Mn	0.089	0.097	0.093	0.083	0.087	0.079	0.084	0.082	0.087	0.087
Ca	1.775	1.749	1.761	1.775	1.759	1.762	1.597	1.789	1.753	1.747
Na	0.000	0.000	0.000	0.000	0.000	0.000	0.000	0.000	0.000	0.000
Sum B	1.864	1.845	1.854	1.858	1.846	1.841	1.681	1.870	1.841	1.833
Na	0.639	0.656	0.634	0.663	0.667	0.669	0.604	0.657	0.664	0.650
K	0.338	0.333	0.308	0.329	0.317	0.329	0.307	0.342	0.321	0.325
Sum A	0.977	0.990	0.942	0.991	0.985	0.998	0.910	0.999	0.985	0.975
Total	15.977	15.989	15.941	15.991	15.985	15.998	15.911	15.999	15.984	15.975
Mg#	0.455	0.457	0.457	0.469	0.469	0.470	0.468	0.471	0.465	0.465
XFe	0.545	0.543	0.543	0.531	0.531	0.530	0.532	0.529	0.535	0.535

**B.4.**

No.	1	2	3	4	5	6	7	Av.
SiO <sub>2</sub>	63.41	63.49	63.54	63.33	64.09	63.67	64.06	63.66
TiO <sub>2</sub>	0.04	0.04	0.01	0.04	0.05	0.03	0.05	0.04
Al <sub>2</sub> O <sub>3</sub>	22.37	22.18	21.99	21.99	22.12	22.12	22.18	22.14
Cr <sub>2</sub> O <sub>3</sub>	0.00	0.00	0.00	0.00	0.00	0.00	0.00	0.00
FeO <sub>t</sub>	0.15	0.08	0.10	0.11	0.03	0.03	0.09	0.08
MnO	0.02	0.02	0.00	0.02	0.00	0.01	0.00	0.01
MgO	0.00	0.00	0.00	0.00	0.00	0.00	0.00	0.00
CaO	4.03	3.66	3.34	3.83	3.51	3.57	3.68	3.66
Na <sub>2</sub> O	8.84	8.84	8.84	8.65	9.04	9.11	8.89	8.89
K <sub>2</sub> O	0.32	0.31	0.24	0.33	0.24	0.31	0.25	0.29
Total	99.18	98.63	98.06	98.31	99.08	98.85	99.20	98.76
Cations per 8 oxygens								
Si	2.836	2.854	2.873	2.861	2.866	2.851	2.865	2.858
Ti	0.001	0.001	0.000	0.002	0.002	0.001	0.002	0.001
Al	1.179	1.175	1.172	1.171	1.166	1.167	1.169	1.171
Cr	0.000	0.000	0.000	0.000	0.000	0.000	0.000	0.000
Fe <sup>3+</sup>	0.000	0.000	0.000	0.000	0.000	0.000	0.000	0.000
Fe <sup>2+</sup>	0.006	0.003	0.004	0.004	0.001	0.001	0.003	0.003
Mn	0.001	0.001	0.000	0.001	0.000	0.001	0.000	0.000
Mg	0.000	0.000	0.000	0.000	0.000	0.000	0.000	0.000
Ca	0.193	0.176	0.162	0.185	0.168	0.171	0.176	0.176
Na	0.767	0.771	0.775	0.758	0.784	0.791	0.771	0.774
K	0.018	0.018	0.014	0.019	0.014	0.018	0.014	0.016
Xan	0.197	0.183	0.170	0.193	0.174	0.175	0.183	0.182
Xab	0.784	0.799	0.815	0.787	0.812	0.807	0.802	0.801
Xor	0.018	0.019	0.015	0.020	0.014	0.018	0.015	0.017

**B.5.**

No.	Biotite						Iron-rich biotite		
	1	2	3	4	5	Av.	1	2	Av.
SiO <sub>2</sub>	37.18	37.15	37.50	37.09	37.02	37.19	37.61	38.28	37.95
TiO <sub>2</sub>	4.36	4.31	4.17	3.80	3.70	4.07	0.25	0.13	0.19
Al <sub>2</sub> O <sub>3</sub>	13.11	13.28	13.42	13.00	13.02	13.17	12.81	12.62	12.72
Cr <sub>2</sub> O <sub>3</sub>	0.01	0.04	0.00	0.05	0.00	0.02	0.03	0.03	0.03
FeO <sub>t</sub>	19.52	19.08	18.92	18.71	18.69	18.98	23.14	22.87	23.01
MnO	0.37	0.34	0.35	0.33	0.31	0.34	0.34	0.40	0.37
MgO	11.55	11.88	11.55	12.56	12.71	12.05	11.43	11.70	11.57
CaO	0.00	0.06	0.06	0.00	0.01	0.03	0.18	0.04	0.11
Na <sub>2</sub> O	0.05	0.08	0.10	0.10	0.11	0.09	0.00	0.00	0.00
K <sub>2</sub> O	10.45	10.28	10.13	10.08	10.09	10.21	10.09	10.15	10.12
Total	96.61	96.49	96.21	95.71	95.67	96.14	95.89	96.22	96.05
Cations per 11 oxygens									
Si	2.899	2.889	2.924	2.887	2.880	2.896	2.938	2.971	2.955
Ti	0.256	0.252	0.244	0.222	0.216	0.238	0.015	0.008	0.011
Al <sup>IV</sup>	1.101	1.111	1.076	1.113	1.120	1.104	1.062	1.029	1.046
Al <sup>VI</sup>	0.104	0.106	0.157	0.079	0.073	0.104	0.118	0.126	0.122
Cr	0.001	0.002	0.000	0.003	0.000	0.001	0.002	0.002	0.002
Fe <sup>3+</sup>	0.000	0.000	0.000	0.000	0.000	0.000	0.000	0.000	0.000
Fe <sup>2+</sup>	1.273	1.241	1.234	1.218	1.216	1.236	1.512	1.485	1.498
Mn	0.025	0.022	0.023	0.021	0.021	0.022	0.023	0.026	0.024
Mg	1.342	1.377	1.342	1.457	1.474	1.398	1.331	1.354	1.342
Ca	0.000	0.005	0.005	0.000	0.001	0.002	0.016	0.003	0.009
Na	0.008	0.013	0.016	0.016	0.016	0.014	0.000	0.000	0.000
K	1.039	1.020	1.007	1.001	1.001	1.014	1.006	1.005	1.005
H	2.000	2.000	2.000	2.000	2.000	2.000	2.000	2.000	2.000
Mg#	0.513	0.526	0.521	0.545	0.548	0.531	0.468	0.477	0.473
XFe	0.487	0.474	0.479	0.455	0.452	0.469	0.532	0.523	0.527

**B.6.**

No.	1	2	3	4	5	Av.
SiO <sub>2</sub>	0.09	0.02	0.01	0.05	0.03	0.04
TiO <sub>2</sub>	51.78	51.78	51.06	52.05	51.71	51.68
Al <sub>2</sub> O <sub>3</sub>	0.02	0.00	0.00	0.00	0.02	0.01
Cr <sub>2</sub> O <sub>3</sub>	0.00	0.03	0.02	0.00	0.00	0.01
FeO <sub>t</sub>	40.71	40.37	40.79	41.22	41.33	40.88
MnO	7.28	7.11	6.89	7.01	6.79	7.02
MgO	0.00	0.03	0.00	0.00	0.00	0.01
CaO	0.03	0.01	0.05	0.00	0.00	0.02
Na <sub>2</sub> O	0.03	0.00	0.04	0.00	0.01	0.01
K <sub>2</sub> O	0.00	0.00	0.00	0.00	0.00	0.00
Total	99.93	99.36	98.85	100.33	99.89	99.67